FOI

Experimental evaluation of two Ku-band conformal antenna arrays

LARS PETTERSSON, LARS-GUNNAR HUSS, RONNY GUNNARSSON,
OLOF LUNDÉN, STIG LEIJON, ANDREAS GUSTAFSSON

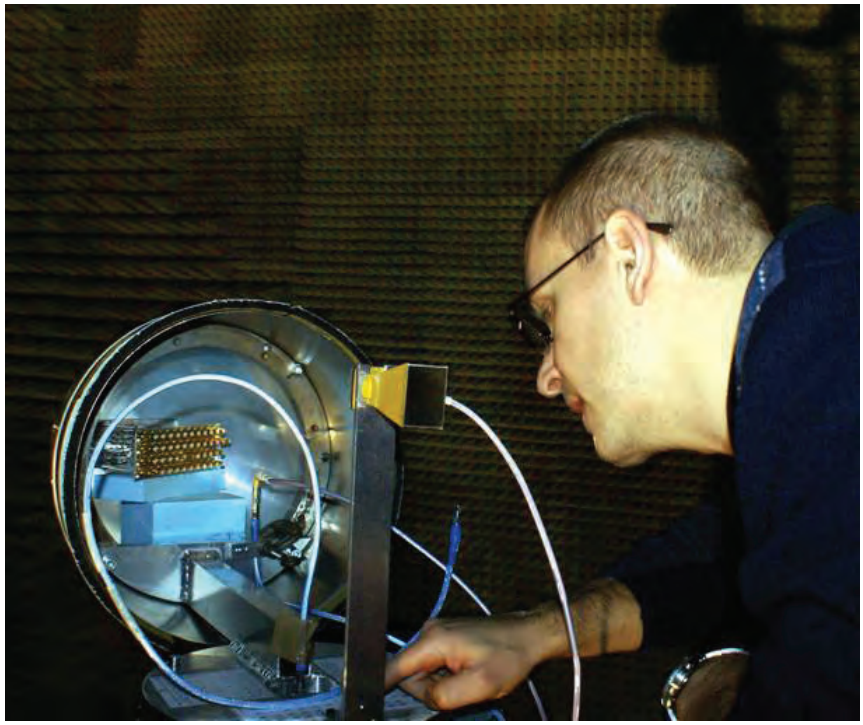

FOI-R--3323--SE Scientific report
ISSN 1650-1942 December 2011

Information Systems

Lars Pettersson, Lars-Gunnar Huss, Ronny Gunnarsson, Olof Lundén, Stig Leijon, Andreas Gustafsson

Experimental evaluation of two Ku-band conformal antenna arrays

Titel	Experimentell utvärdering av två Ku-bands konforma gruppantenner
Title	Experimental evauation of two Ku-band conformal antenna arrays
Rapportnr/Report no	FOI-R--3323--SE
Rapporttyp/ Report Type	Vetenskaplig Rapport
Sidor/Pages	51 p
Månad/Month	December
Utgivningsår/Year	2011
ISSN	ISSN 1650-1942
Kund/Customer	Försvarsmakten
Projektnr/Project no	E53045
Godkänd av/Approved by	

FOI, Totalförsvarets Forskningsinstitut
Avdelningen för Informationssystem
Box 1165
581 11 Linköping

FOI, Swedish Defence Research Agency
Information Systems
Box 1165
SE-581 11 Linköping

Sammanfattning

Två olika konforma gruppantenner för frekvensbandet 16 – 18 GHz har byggts, monterats på en UAV-nosattrapp, och utvärderats experimentellt. En gruppantenn är fasetterad med fem plana delantenner med 7×7 antennelement vardera och den andra är mjukt krökt med 35×7 antennelement Båda gruppantennerna har identiska probmatade mikrostripelement.

Strålningsdiagram för några utvalda antennelement har mätts och analyserats. Både systematiska och till synes slumpässiga variationer kan ses. Eftersom de flesta element i den mjukt krökta gruppantennen sitter i mer lika omgivning uppvisar de något bättre kvalitet på diagrammen men diagramkvaliteten för båda gruppantennerna anses dock fullt adekvat för att kunna forma totala gruppantenndiagram av hög kvalitet. De mätta elementdiagrammen har också använts i ett visualiseringsverktyg för att bilda totala strålningsdiagram.

Nyckelord: konform gruppantenn, antennmätning, mikrostripantenn, fasetterad gruppantenn, mjukt krökt gruppantenn

Summary

Two different conformal arrays for the frequency band 16 – 18 GHz have been built, mounted on an UAV nose mock-up, and evaluated experimentally. One array is facetted with five planar subarrays of 7×7 antenna elements each and the other is smoothly curved with 35×7 antenna elements. Both arrays have identical probe fed microstrip elements.

Patterns of selected antenna elements have been measured and analyzed. Both systematic and a random-like variations can be seen. Since most of the elements in the smoothly curved array are in a more similar environment they show slightly higher pattern quality but the pattern quality of both arrays is considered adequate to produce good total array patterns. The measured element patterns have also been used in a visualization tool to form complete array patterns.

Keywords: conformal array, antenna measurement, microstrip antenna, faceted array, smoothly curved array

Table of contents

1 Introduction

This report discusses the experimental evaluation of two Ku-band conformal antenna arrays, one faceted with five planar subarrays with 7×7 elements each and one smoothly curved with 35×7 elements. Both arrays have identical microstrip elements. The results have partly been previously reported in the conference papers, [1], [2] and [3], but here a more complete and detailed account of the work and results are given.

Conformal antenna arrays have radiating elements that are in some way mounted on, or integrated with, a curved surface. Advantages are a wider field of view and that less internal space is required. The integration can be done smoothly, such as on a circular cylinder or a sphere, or faceted using small planar subarrays. Both types have been built and tested and both consist of a total of 35×7 elements which are mounted on a hemispherical UAV nose mock-up with 30 cm diameter. The elements are probe fed, single polarized, quadratic microstrip patches which are easy to manufacture. To make relevant numerical calculations on the whole array on the mock-up is a major task and is not considered feasible.

There are some standard assumptions, valid for large planar arrays, which we can not rely on for non-planar arrays. For planar arrays with no grating lobes the embedded element patterns are often approximated as that for an infinite planar periodic array, i.e. $G(\theta,\varphi)\propto\cos\theta\left(1-\left|\Gamma(\theta,\varphi)\right|^2\right)$ where $\Gamma(\theta,\varphi)$ is the active reflection coefficient for a scanned beam. In a real finite array this is altered by the array edges, manufacturing tolerances and reflections from non-identical feeding circuits. There are also other symmetry properties which are valid for infinite planar arrays but not for finite array and even less for non-planar, finite, arrays. The deviation between infinite planar arrays and non-planar, in particular double curved, arrays is further stressed in that the latter have no strict periodicity.

Phase and polarization is not given by any similar simple equations but this is often not important since they all equal for are elements in a planar infinite array. In a non-planar array however it may in general be very important. When the array curvature is small, the planar array properties may be good approximations but, since the elements are pointing in different directions, the radiation phase and polarization is more critical and will directly influence the array radiation pattern. Hence a good knowledge of the element patterns is desired.

All of the above mentioned differences make an experimental evaluation of a non-planar array more motivated. Looking on the arrays from a practical viewpoint, conformal arrays are also often more complex to manufacture with high precision. Mechanical discontinuities in ground plane and substrates are also more likely to be present. All this will affect the array performance and also add to the motivation of experiments.

In a circular array the element patterns will be independent of azimuth position however and we will use this fact to obtain a quality measure of our manufacturing and measurements.

An experimental evaluation is not very easy to perform if we want high accuracy. The mechanical structure is rather bulky and heavy, making mechanical deformations and vibrations an issue. Also the measurements take relatively long time, about one day for an element, so stability in the instruments is also critical. The truncation and realism of the structure, a UAV mock-up in this case, is another issue. Furthermore the manufacturing and integration of the arrays and elements are critical and not very easy so we must expect each element, with its connecting probe and matching load, to be individuals with slightly “random” characteristics as indeed they will be in an operational array.

In all however we have good confidence in the results and that they give indeed a good picture of the array performance provided one does not try to look too much in the small details.

2 Design of the element and arrays

2.1 Mock-up of a UAV-nose and measurement set up

The UAV nose mock-up is made as a hemisphere of diameter 304 mm with the radius to the center of the facet ground planes being 145.6 mm. Drawings of this and the mounting fixtures used for the faceted array is shown in Figure 1 and Figure 2. Before the smoothly curved array was mounted the angularity of the faceted structure was milled away to form a cylindrical structure with the radius 145.6 mm. Behind this hemisphere there is a, slightly conical, 150 mm long extension as seen in Figure 1. During the measurements this extension was covered with absorbing material as shown in Figure 3 to reduce diffraction from its edge as much as possible. (In a real UAV this edge is of course not present at all.) In Figure 1 we can also see a vertical arm behind the mock-up which is used for mounting a small reference horn.

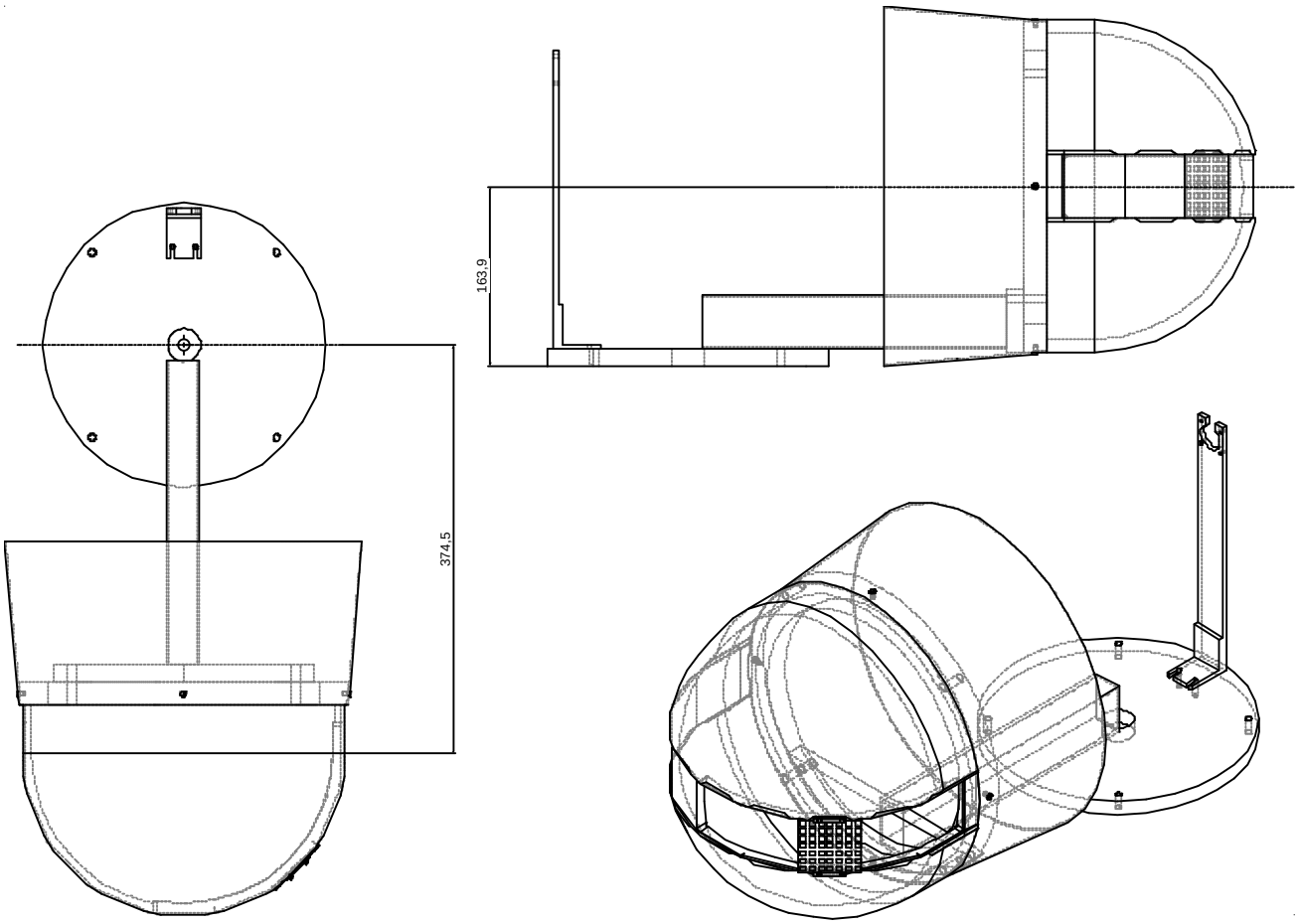

Figure 1 Drawing of UAV nose mock-up and test fixture.

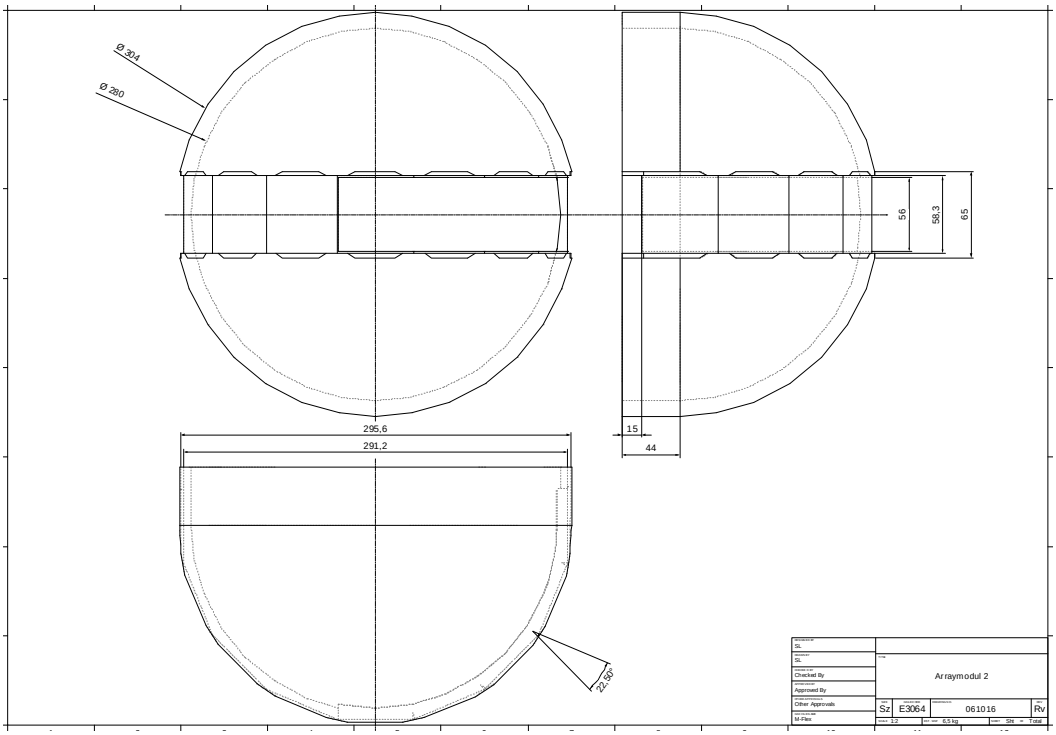

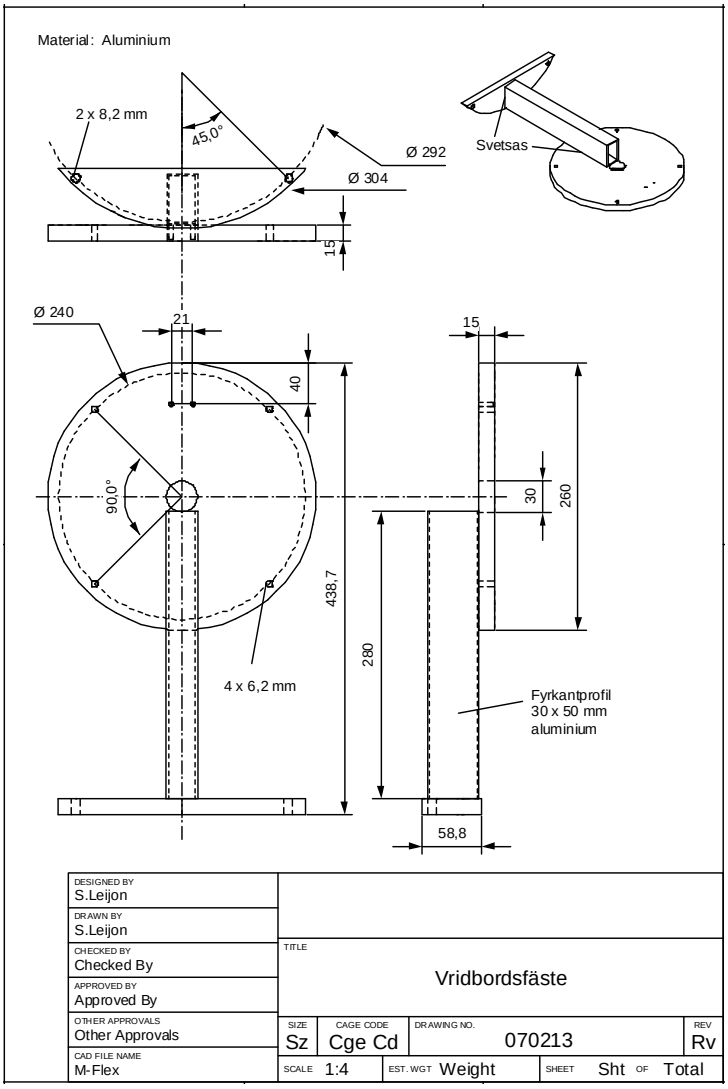

Figure 2 Drawings of spherical shell and mounting fixture.

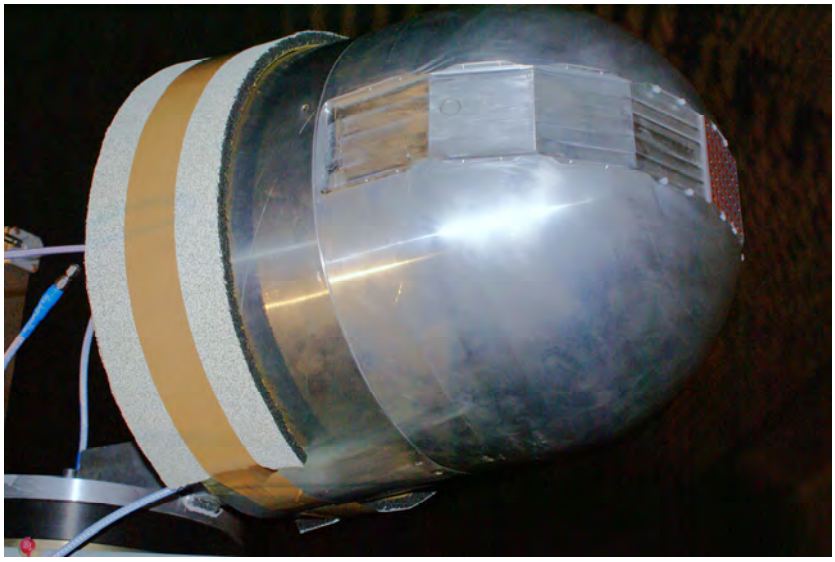

Figure 3 The right hand side, without antenna elements, with absorber shown.

For the faceted array measurements, five subarrays, one “active” with cable attached to the elements and four passive, terminated with chip resistors, were mounted on a 90° sector the left hand side, from the forward pointing direction to the side pointing direction, numbered as in Figure 4. Measurements were done with the active subarray sidelooking and the two neighboring subarray positions (no 3, 4 and 5 in Figure 4) and the empty positions on the other side of the nose, seen in Figure 3, were not used.

When the faceted array had been measured the mock-up was modified by milling down the faceted structure making it circular cylindrical as discussed above. (We are thus not able to return to the faceted structure again.)

The smooth array was made as a long array which was bent down to this cylindrical surface, covering the same angular interval as the faceted, as seen later in Figure 15 in section 2.4.

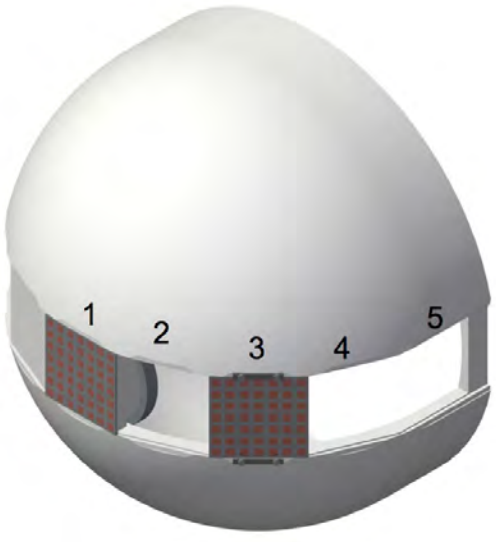

Figure 4 Numbering of the facet positions, with arrays in two of the facet positions only.

2.2 Antenna element

The antenna element used in both arrays discussed was a simple and low cost probe fed microstrip patch antenna described in Figure 5 and Figure 6. Elements with wider bandwidth and also with dual polarizations can be designed and built. Our aim was however to study the effects of non-planarity of the arrays and not the elements themselves and thus did not want to spend too much effort and time on a more complex element. It is designed to work in the upper Ku band, between 16 to 18 GHz. The lattice is quadratic with a period of 8.33 mm ($\lambda/2$ at 18 GHz) in both directions. Since the elements, array grid and also the planar facets are quadratic, we can study both horizontal and vertical polarized elements in the faceted array by simply rotating the subarrays 90°. In the smooth array however only horizontal polarized element has been used.

The element design is shown in Figure 5 and Figure 6 and the active reflection coefficient in an infinite array for various beam pointing, calculated with the HFSS software, is shown in Figure 7.

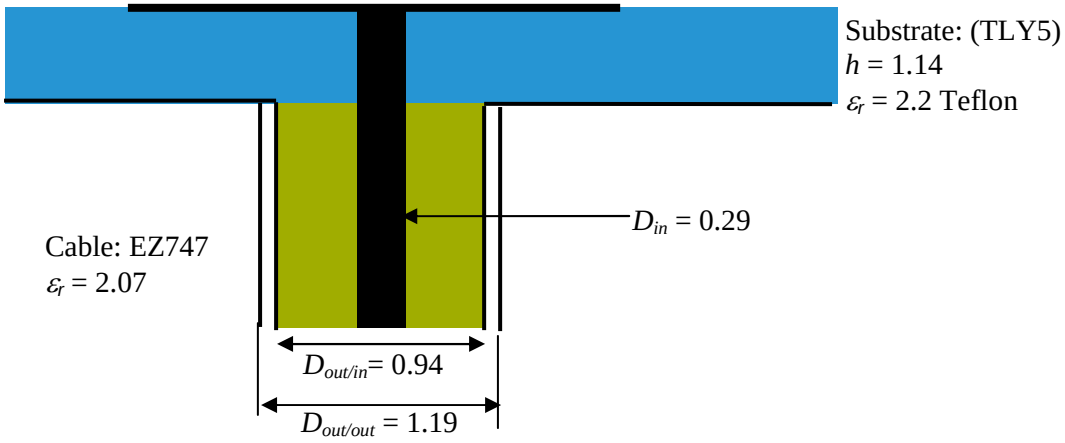

Figure 5 Schematic view of the probe connection. Dimensions in mm.

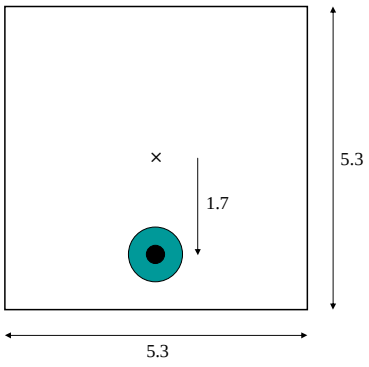

Figure 6 Lay-out of the patch. Dimensions in mm.

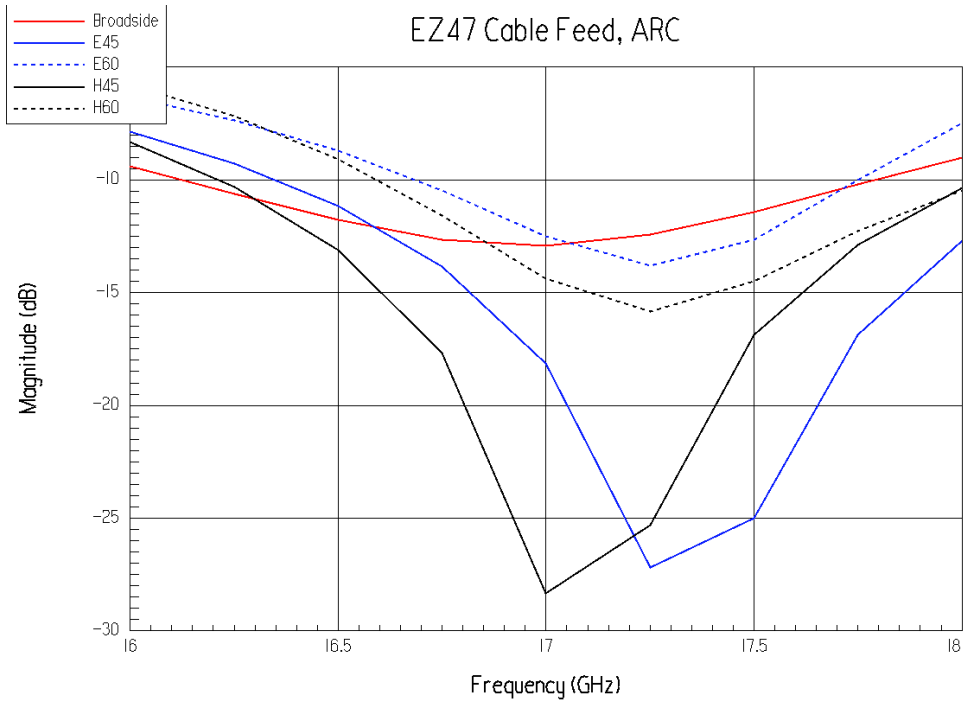

Figure 7 Active reflection coefficient for an infinite array calculated by HFSS. Broadside and two E and H plane scans.

2.3 Planar subarray

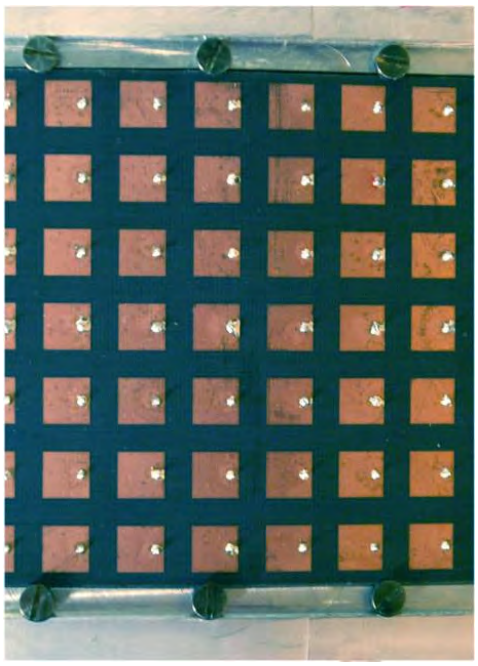

Figure 8 A 7×7 patch subarray held down to the mock-up by the edge of the screw heads.

To be able to rotate the subarray 90° to change polarization, the subarray are made as squares. This is the reason for the small distance from the edge elements to the substrate edge (half element spacing from element center to substrate edge) seen in Figure 8. Also, due to space limitations, there were no coaxial cables connected to the corner elements but the elements were terminated with 50 Ω chip resistors (RG1025-50P0-5).

A drawing of the back up plate for the active faceted subarray is given in Figure 9. On this the active subarray is mounted and we can see all $7 \times 7 - 4 = 45$ holes for the 1.19 mm coaxial cables.

When mounted as in Figure 8 and with the subarray in position 5 the feeding probes are close to the array end. To also measure the case when the feeding probes are on the other side of the patch, away from the array edge, the subarray was also measured when turning it “up-side down” as shown in Figure 10.

A close up picture of a subarray is shown in Figure 8 and the mock-up with five subarrays is shown in Figure 11. Only one of the subarrays shown is “active”, i.e. with coaxial cables attached, while the others are “passive”, with no coaxial cables attached, (to decrease the complexity and cost) as seen in the view from the inside in Figure 12. All elements in these passive subarrays were also terminated by the chip resistors. Figure 12 also shows the copper tape used to secure a good electrical connection between the facet ground planes.

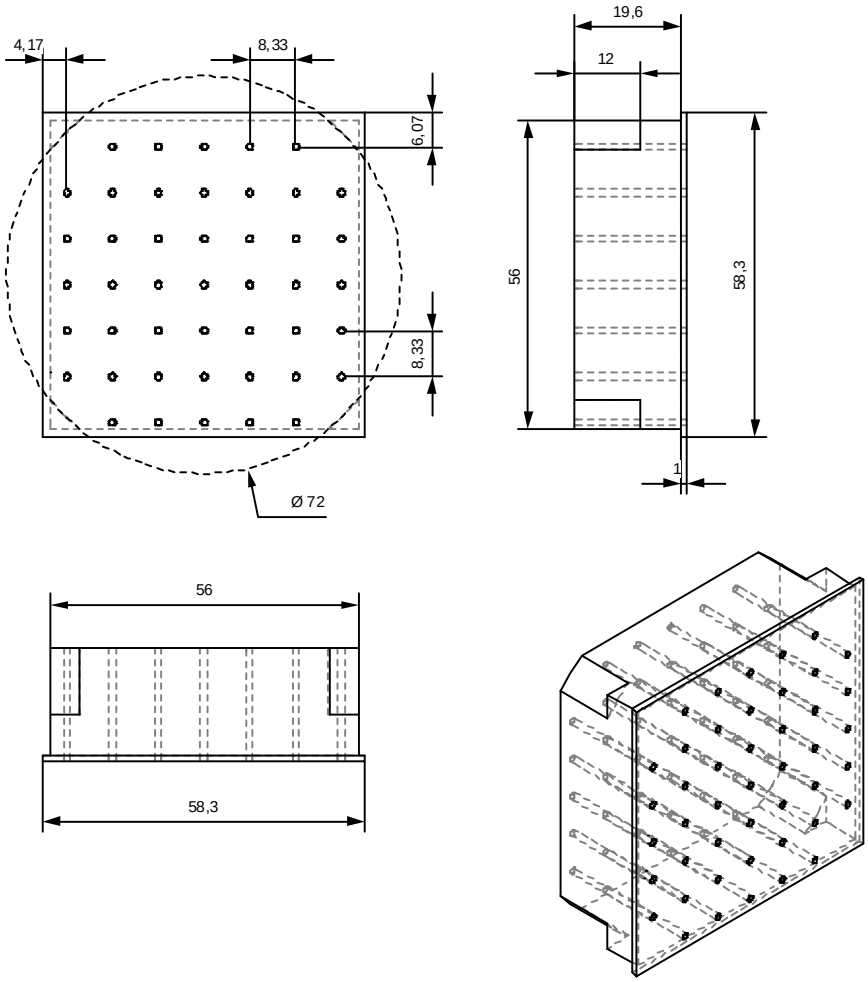

Figure 9 Drawing of back up plate.

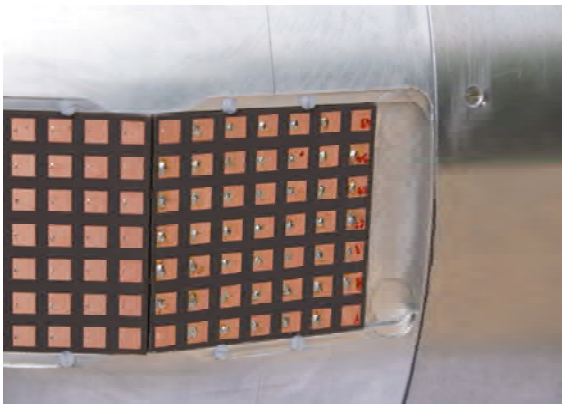

Figure 10 Subarray mounted upside down in position 5

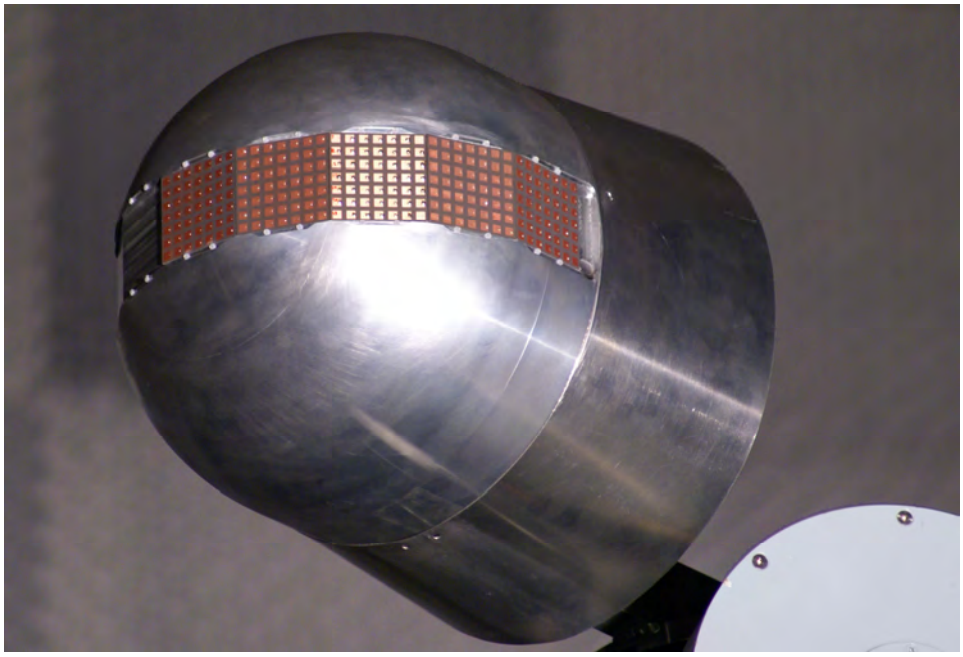

Figure 11 Mock-up with horizontal polarization elements.

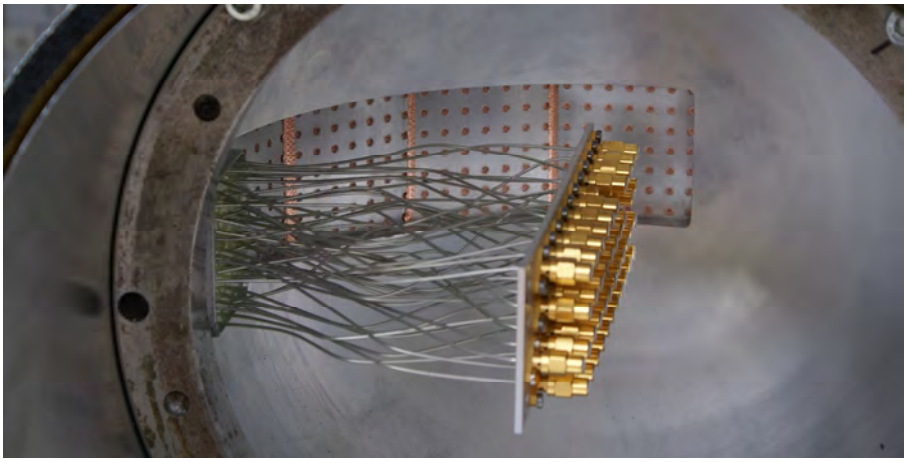

Figure 12 One active and four passive subarrays seen from the back side when measuring subarray position 5. Two elements measured and 43 terminated by coaxial load and 200 by 50 Ω chip resistors.

The measured patterns, presented later, may also be compared with calculated patterns. Figure 13 shows patterns of the 7×7 element array, i.e. an isolated facet, with an infinite ground plane, calculated using the finite difference time domain, FDTD, method.

The feeding probe is on the right hand side of the patches, as in most of the measured patterns. This array is of course too small to represent the full array but some comparisons can be made. The general behavior is similar to both of the measured arrays except for the edge element where the very strong gain decrease on the left side of the plot is much smaller in the calculated results. The reason for this is yet unclear but the two measured arrays differed mostly here and the actual design of the attachment to ground may be the reason.

The total radiated fields from elements in an isolated subarray have also been calculated and a “slice” showing the radiated waves is shown in Figure 14 where we also can see the edge effects.

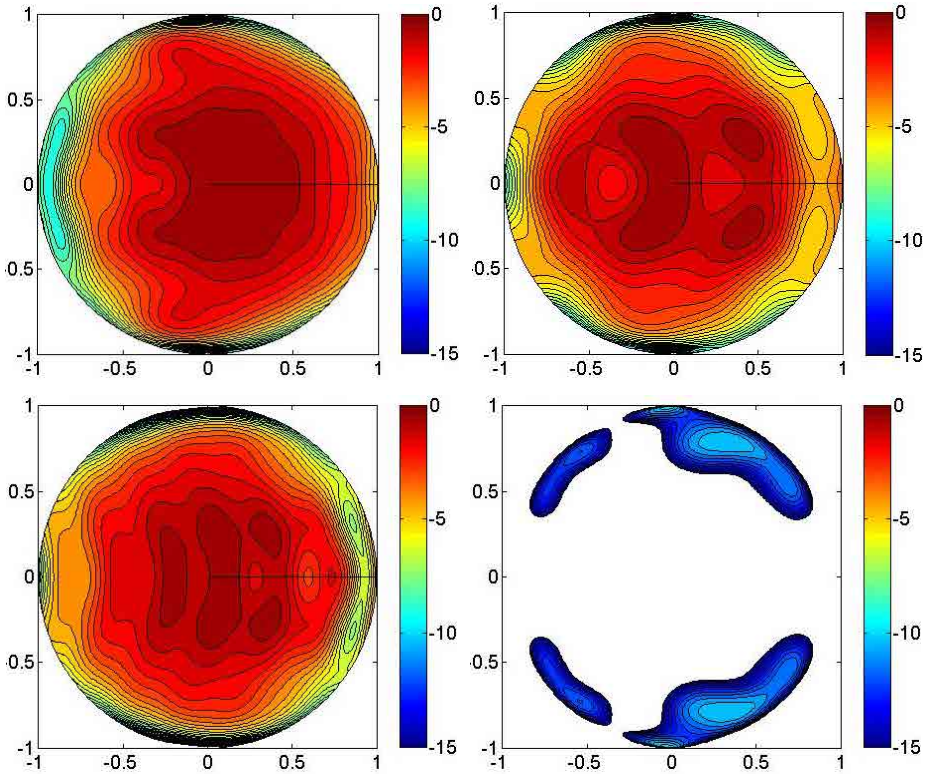

Figure 13 Calculated element patterns at 17 GHz for elements in a 7×7 element isolated facet as in Figure 8. Co-polarization for element at the right edge (upper left), in the center (upper right), at the left edge (lower left), and cross-polarization for the center element (lower right).
The axes of the plots are the direction cosines, $v = \sin\theta \sin\varphi$ and $w = \cos\theta$.

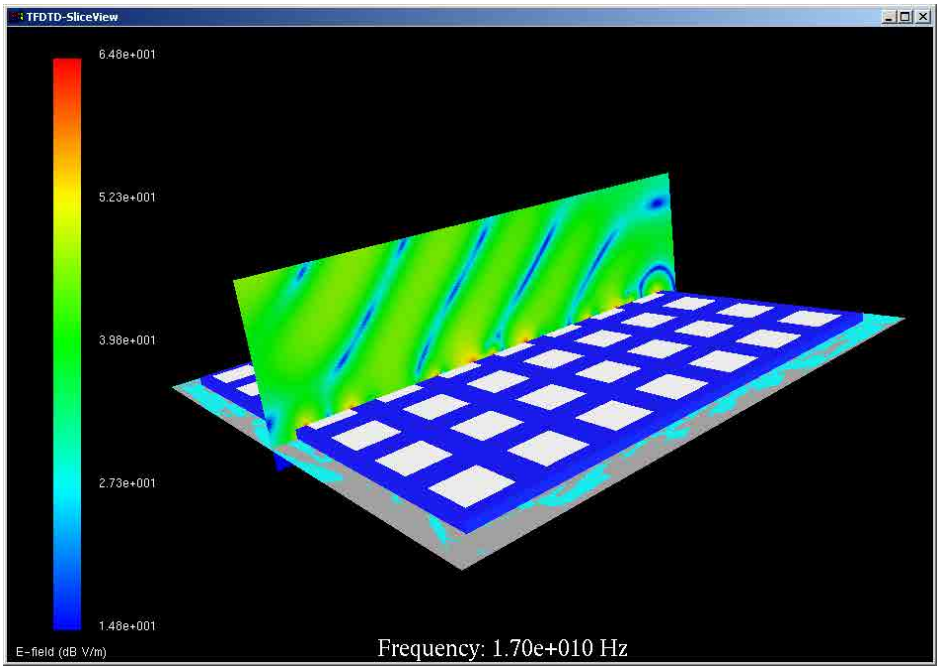

Figure 14 Snapshot of the electric field radiated from a 7x7 array obtained from a FDTD simulation. Beam steered 45° in the E-plane.

2.4 Smoothly curved array

The elements of the smoothly curved array in Figure 15 are identical to those of the faceted array. Thus measurement results should be directly comparable. Only an array for horizontal polarization has been built and tested however and only the center row of elements is connected to coaxial lines while the other are terminated with 50 Ω chip resistors, see Figure 16.

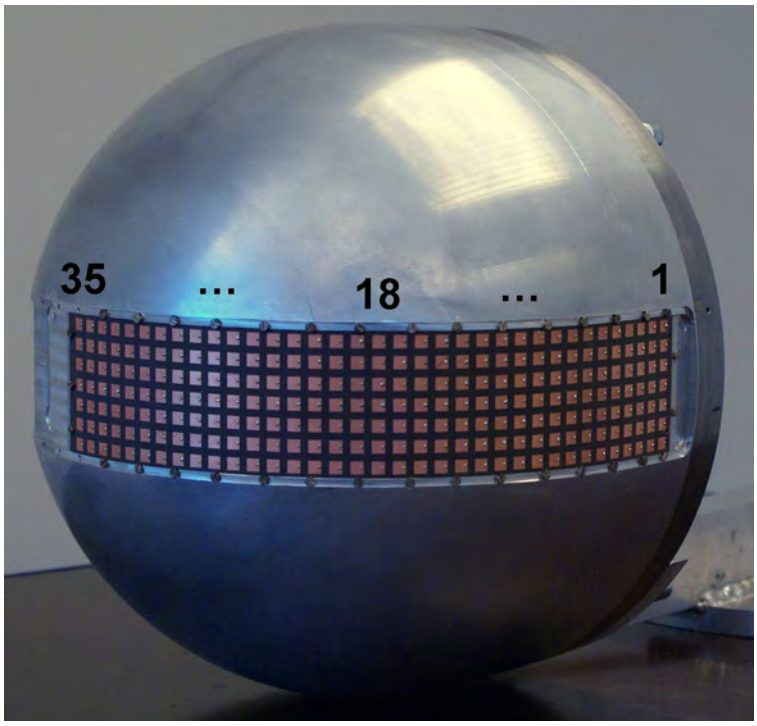

Figure 15 Mock-up with smoothly curved array.

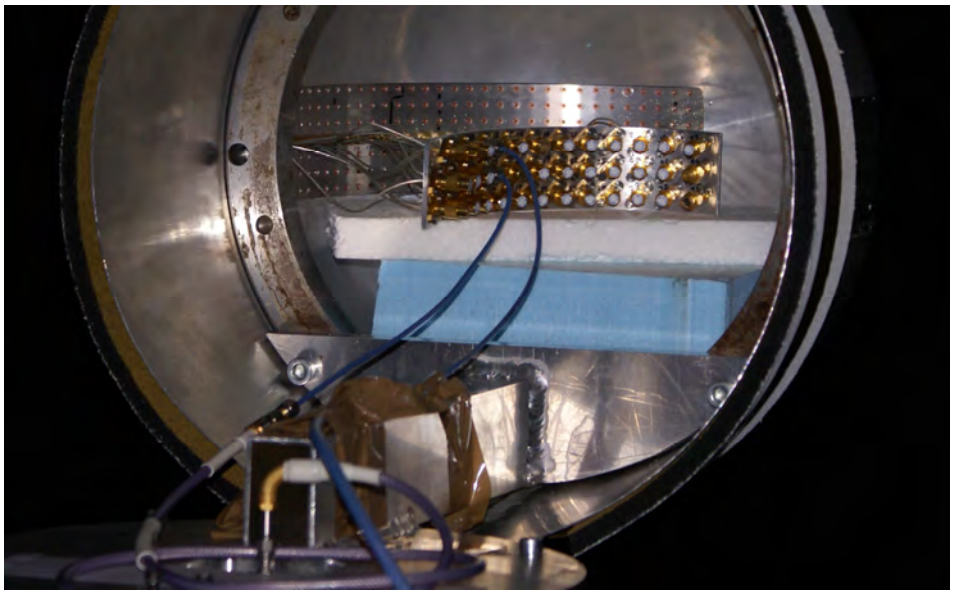

Figure 16 The smoothly curved array seen from the back side. Two elements measured and 33 terminated by coaxial load and 210 by 50 Ω chip resistors.

3 Measurements

3.1 Procedure

Embedded element patterns of the two arrays on an UAV nose mock-up have been measured in the large anechoic chamber at FOI. The mock-up was mounted on an arm, discussed in section 2.1, on top of an azimuth-over-elevation positioner as shown in Figure 17. The receiver has two parallel channels which were both used. This doubles the measurement speed. One channel is fed through the rotational joints while the other is fed through a cable that is hanging freely, as may be seen in Figure 17. We have not seen any negative effects of this, e.g. phase shifts due to cable bending. The mixers of the measurement system are positioned below the top positioner, hanging in the red straps seen in the figure.

In Figure 17 we can also see a small rectangular horn pointing in opposite directions relative to the mock-up. This was used as a reference horn and for testing the stability of the set up when desired. The co polarization plots shown in this report are all normalized at broadside but the calibration is required to connect the H and V polarization data to each other.

This type of mounting, and the size of the mock-up, means that the center of rotation is not where we ideally want it to be, in the center of the patches. This is however partly be corrected for.

Important parameters in this correction are, based on drawing parameters:

- Vertical distance from horizontal axis to azimuth plate surface: 140 mm
- Vertical distance from azimuth plate surface to center of mock-up sphere: 168 mm
- Distance from vertical axis to center of mock-up sphere along center line: 374.5 mm
- Radius of mock-up sphere to inner surface of array attachment: 145.6 mm

To this should be added:

- An perpendicular off set due to a misalignment of the mounting arm: 4 mm
- Thickness of the faceted array mounting plate: 1 mm
- Thickness of curved array mounting plate etc. (Ideally to the neutral line of the bend.) 2.4 mm

There is also some small misalignments and bending of the structure. Since the wavelength is about 18 mm a position tolerance of 0.1 mm will give a phase error of up to 2°. The remaining “alignment” can be thought of as a calibration (which should be made in all real arrays anyway) and is here done by inserting a fix (the same for all elements and subarrays) offset angles in azimuth and elevation to make the element phase patterns approximately symmetrical. The resulting offset angles were found to be:

- Offset in elevation for faceted and smooth array: –0.3°
- Offset in azimuth for faceted array: –0.2°
- Offset in azimuth for smooth array: 0°

The distance from the center of rotation to an element is approximately 0.5 m. There will thus also be a parallax error so that the angle from the element surface normal to the transmitting antenna is different than what is directly obtained from the positioner. The measurement distance is $R_{Meas} = 25$ m so that errors will be up to 1° approximately. Since the element patterns are relatively broad and smooth in both magnitude and phase when we use the element center as center of reference, this parallax error has not been corrected for.

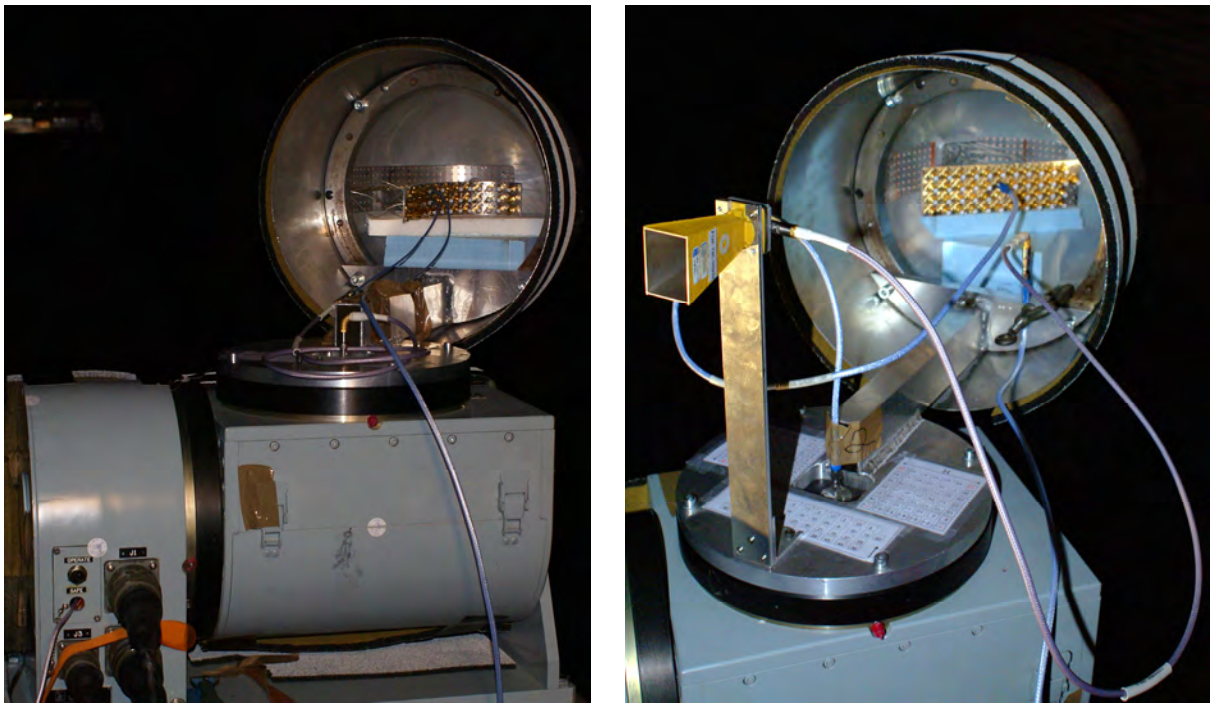

Figure 17 The UAV mock-up on the positioner seen from the back side. The smoothly curved array left and the faceted array right. A small reference horn is also seen.

3.2 Reduction of raw data to element centered data

To be more easily evaluated and usable in antenna analysis and pattern synthesis the data should be referred to the elements themselves, preferable to a local coordinate system centered in the element center. The measured raw data are however referred to a global, array fixed, coordinate system with origin in the center of rotation. The z-axis of the global system is the axis of the azimuth turntable and the x-axis is the symmetry line of the UAV mock-up while the local coordinate systems has their z-axis in the element plane, parallel to the global z-axis and their x-axes perpendicular to the element surfaces. The data should thus be transformed from this global to each local coordinate system.

The elevation positioner will thus control the global θ-angle, the azimuth positioner the global φ-axis and the measured V and H polarizations will be the θ and φ polarizations respectively.

The phase should be corrected by subtracting the phase due to the element center not being the center of rotation. Let the element center expressed in the global, array fixed, coordinate system be $\mathbf{r}_{el}$, the measurement distance from the center of rotation to the illuminating antenna in the chamber be R_{meas} and the directions to this antenna in the global coordinate system be (θ, φ) where $\theta = 90° - Elevation$ and $\varphi = Azimuth$ is the angles obtained from the two positioner axes, being of course corrected for the angular offsets given in section 3.1. The difference in distances from the illuminating antenna to the origins of the local and global coordinate systems is

$$dR = R_{el} - R_{Meas} = \sqrt{R_{Meas}^2 + |\mathbf{r}_{el}|^2 - 2R_{Meas}\hat{k}\cdot\mathbf{r}_{el}} - R_{Meas} \approx -\hat{k}\cdot\mathbf{r}_{el}$$

where $\hat{k} = (\sin\theta\cos\varphi, \sin\theta\sin\varphi, \cos\theta)$.

The amplitude may be corrected for by a factor R_{el}/R_{Meas}. This is close to one and has not been included.

There is also a small parallax error, due to the finite measurement distance, making the local angles different, mostly larger, than those of the global system. This correction is about 1° at most and is neglected

which may be motivated by the slowly varying element patterns, i.e. wide magnitude as well as phase patterns when referred to the local coordinate system. The elements are however rotated but in our geometry the rotation is limited to a rotation of φ_{el0} in azimuth so that $\varphi_{el} = \varphi - \varphi_{el0}$.

The polarization measured is vertical and horizontal which, with the azimuth-over-elevation positioner used, transforms to θ and φ polarizations. The small parallax will give a small rotation of the polarization outside the principal planes but this is also neglected here.

The position coordinates of the elements in the faceted array may, in a coordinate systems parallel to the local systems discussed above but with origin in the sphere center, be written, in Matlab style, as:

$$\mathbf{r}_{elL} = [R_{sub}; D(n_{y,el} - 4); D(n_{z,el} - 4)]$$

where $n_{y,el}$ and $n_{z,el}$ are the element index in each subarray, $R_{sub} = 146.6$ mm is the radius to the center of the facet ground planes plus thickness of the mounting plate (145.6+1) and $D = 8.33$ mm is the element spacing.

In the smoothly curved array the first three measured elements are on the cylindrical part of the mock-up while the other 32 are on the spherical part. The positions of the elements, in coordinate systems parallel to the local systems but with origin in the sphere center, can be written, in Matlab style,

for the first three elements in y-direction, $n_{y,el}$:

$$\mathbf{r}_{elL} = \left[R_{sub}; D\left(4 - n_{y,el}\right) + y_4; D\left(4 - n_{z,el}\right) \right]$$

and for the other 32 elements:

$$\mathbf{r}_{elL} = \left[R_{sub}; 0; D\left(4 - n_{z,el}\right) \right]$$

where $n_{z,el}$ is the element position vertically of which we have only measured number 4 with $z = 0$, $y_4 = 2.35$ mm is the y-coordinate of element number 4, $R_{sub} = 148$ mm is the radius to the curved array mounting plate (145.6+2.4) and $D = 8.33$ mm is the element spacing as above.

Note that when we bend the array, which is made flat, the spacing between the metallic patches may change slightly.

The positions in the global coordinate system is then given by:

$$\mathbf{r}_{el} = \mathbf{R}_0 + \mathbf{T}_{el}\mathbf{r}_{elL}$$

where the vector $R_0 = [374.5; -4; 308]$ mm is the position of the sphere (see previous page) and

$$\mathbf{T}_{el} = \begin{bmatrix} \cos(\varphi_{el0}) & -\sin(\varphi_{el0}) & 0 \\ \sin(\varphi_{el0}) & \cos(\varphi_{el0}) & 0 \\ 0 & 0 & 1 \end{bmatrix}$$

is a transformation matrix where φ_{el0} is the pointing angle of the element in the global system discussed above. The local coordinate axes are given by the columns of $\mathbf{T}_{el}$.

In the faceted array the angles for the different subarray positions are

$$\varphi_{el0} = 22.5(n_{Arr} - 1)\,\pi/180$$

where n_{Arr} is the subarray position, number 1 pointing forward and number 5 to the left side as in Figure 4.

In the smoothly curved array the 35 angles are, written in Matlab style:

$$\varphi_{el0} = \left[90, 90, 90, 90 - \Delta_{\varphi 4} - \Delta_{\varphi} \left[0:31 \right] \right] \pi / 180$$

where $\Delta_{\varphi 4} = 0.9185$ is the angle of element number 4 and $\Delta_{\varphi} = 3.22438$ is the inter-element angular step in degrees.

These transformations illustrate the increased complexity introduced when building and using conformal arrays as compared with planar arrays.

3.3 Choice of measured elements

3.3.1 Faceted array

In the faceted array there are in total 490 possible antenna measurements (2 polarizations, 5 subarray positions, 7×7 subarray elements). With our measurement facilities (having two receiver channels) we can, with the raster scan used, measure two patterns per day. Thus to measure all of the possibilities is in practice impossible but a selection must be made. The selections was made to get representatives of different kinds of surrounding and also a continous center line of measured elements.

Four different subarray position-rotation combinations are measured, numbered as in Figure 4.

With subarray in position 5, at the cylindrical end, with the element probes on the right hand side close to the array edge for nominal H-polarization, Figure 18.

With subarray in position 5, at the cylindrical end, with the element probes on the upper side for nominal V-polarization, Figure 19.

With subarray in position 5, at the cylindrical end, with the element probes on the left hand side away from the array edge for nominal H-polarization, Figure 20.

With subarray in position 4, at the cylindrical end, with the element probes on the right hand side close to the array edge for nominal H-polarization, Figure 21.

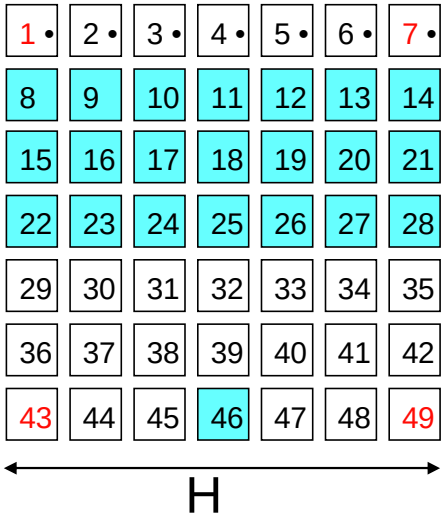

Figure 18 Array position 5. H-polarized elements, probe to the right. Subarray seen from outside. Measured elements blue.

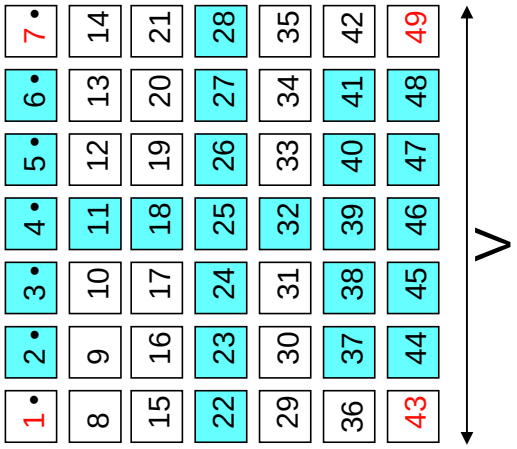

Figure 19 Array position 5. V-polarized elements, probe on the upper side. Subarray seen from outside. Measured elements blue.

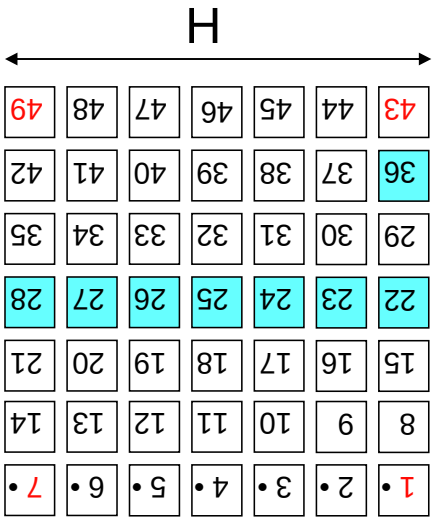

Figure 20 Array position 5. H-polarized elements, probe on the left side. (Panel rotated 180 degrees.) Subarray seen from outside. Measured elements blue.

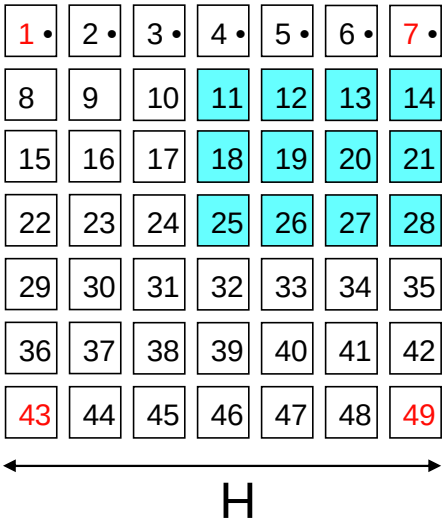

Figure 21 Array position 4. H-polarized elements, probe to the right. Subarray seen from outside. Measured elements blue.

3.3.2 Smoothly curved array

In the smoothly curved array only the elements in the center row have been measured. They are numbered as shown in Figure 22 and Figure 15. Here the elements have the probes at the right hand side for nominal H-polarization, as the faceted subarrays in Figure 19 and Figure 21.

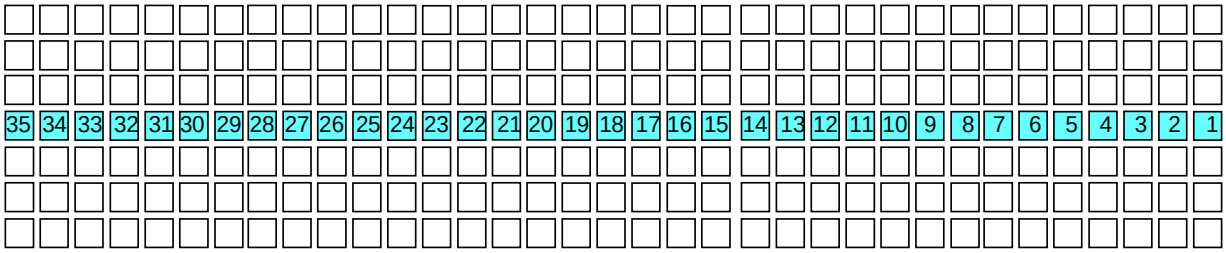

Figure 22 The smoothly curved array flattened out. Probe connections are on the element right side. Subarray seen from outside. Measured elements blue.

4 Measurement results

4.1 Description of the results presented

The element patterns have been measured in a raster scan with the test object mounted on an azimuth-over-elevation positioner as seen in several of the previous pictures. The angular scan was slightly over ±90° in azimuth and up to ±75° in elevation in the local coordinate systems of each element (*z*-axis pointing upward and *x*-axis in element broadside). In the following sections a number of contour plots of the co-polar (along $\hat{\varphi}$ for H-polarized elements) and cross-polar (along $\hat{\theta}$ for V-polarized elements) fields are given. The polarization convention thus follows the Ludwig 2:nd definition, [5]. Apart from being the most practical here (avoiding a transformation to the more commonly used Ludwig 3:d definition) it has the advantage that the $\hat{\theta}$ and $\hat{\varphi}$ vectors point in the same directions are equal for all elements and the global measurement coordinate systems.

The plot coordinates are the direction cosines, $v = \sin\theta\sin\varphi$ and $w = \cos\theta$, with the *x*-axis pointing in element broadside and *z*-axis up in Figure 11 and Figure 15. The magnitudes are normalized to co-polar peak equal to 0 dB and the contour line interval is 0.5 dB with a 15 dB plotting range. Phase plots are normalized to co-polar phase equal to 0 in broadside and the contour line interval is $\pi/36 = 5°$.

Before we measure we need to determine the angular sampling density necessary, where we of course want to sample as sparse as possible.

The elements are positioned up to $R_{max} = 0.5$ m from the center of rotation and to strictly fulfill the sampling criterion the angular sampling would have to be dense, with $\Delta\varphi < 360° \lambda/(4\pi R_{max})$. However, since we want the element patterns in their local coordinate system, we transform the patterns to the patch centers and the "effective radius" of the elements and their surrounding will then be much smaller and the required sampling step larger, making 2.5° steps sufficient.

Theoretically the maximum sampling step is still determined by the smallest surrounding sphere, $\Delta\varphi < 360°/(2N+1)$ where the highest mode is given by $N = kR + n_1$ (R being the radius of the smallest surrounding sphere and n_1 an extra margin), but as discussed below in Figure 23 the higher order mode amplitudes are low.

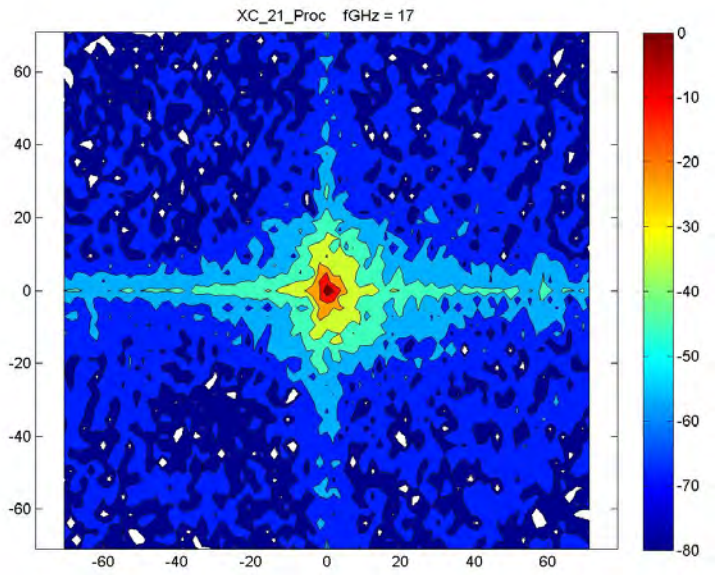

Figure 23 Angular spectrum vs. Fourier indices of measured φ-polarized element pattern for element 21 in the smooth array in Figure 15, transformed to the patch center. $f = 17$ GHz. 10 dB contour steps.

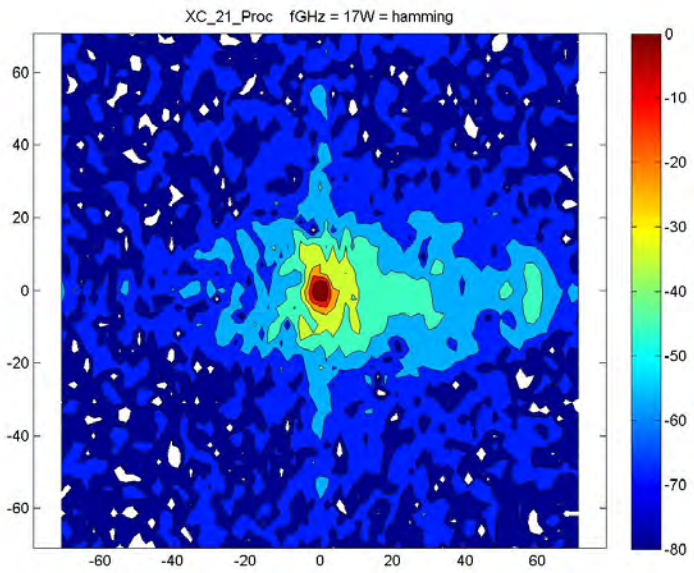

Figure 24 Same as Figure 23 but with a Hamming window applied in the transformation.

This transformation does of course require detailed knowledge of the position and pointing of each element, as discussed in section 3.2. This coarser sampling will also mean that any, presumably small, scattering from far off edges, positioner, mast etc. will not be properly measured but this is considered acceptable. The UAV-nose is attached to a skirt with absorbers (skirt but not absorbers seen in Figure 3) to reduce its scattering.

As an example, the result from taking an FFT of the φ-polarized pattern in φ- and θ-directions (not spherical harmonics) of an element in the center of the array, at 17 GHz, is shown in Figure 23 and, when also applying a Hamming window, in Figure 24. The scales indicates the angular indices, i.e. m in $\exp\left(jm\varphi \right)$.

As seen, most power is concentrated in the center with small ridges in the horizontal and vertical directions in the un-windowed spectrum, Figure 23, indicating array lattice and edges but also the sample truncation. When a Hamming window is used, Figure 24, these ridges are essentially removed but the spectral magnitude is still somewhat larger for positive φ-indices.

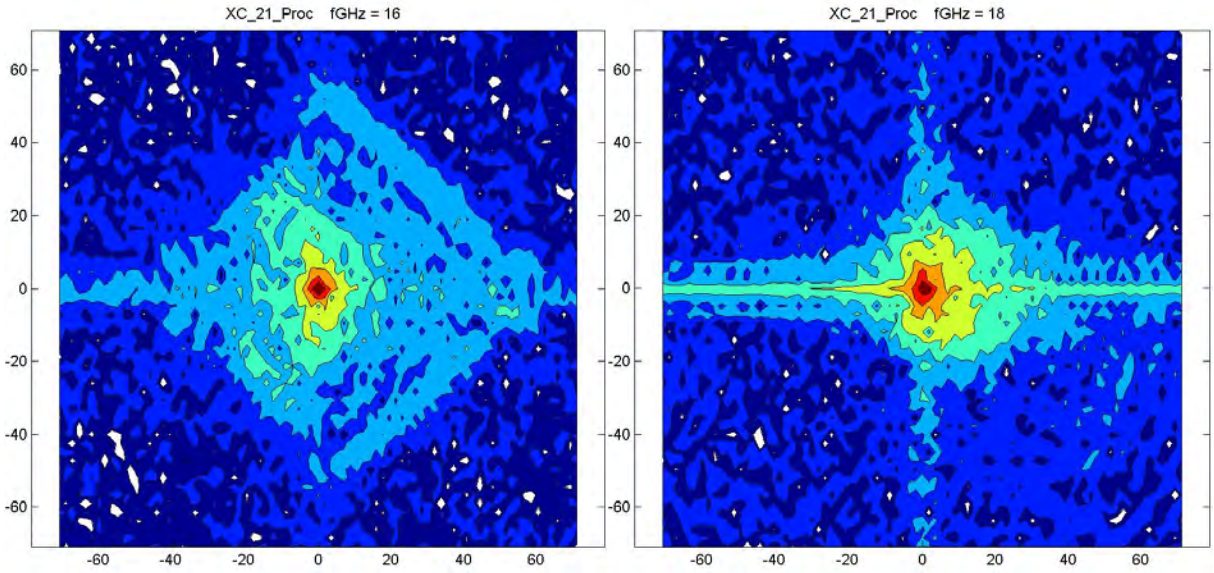

Figure 25 Same as Figure 23 but for 16 and 18 GHz respectively.

The spectra for the band edges, 16 and 18 GHz, is shown in Figure 25. At 16 GHz there is a rhombic like floor between –50 and –60 dB which probably is related to the wavy structure of the pattern, as seen for element 18, in particular for wide angles, in Figure 50. The origin of this ripple is yet unknown. At 18 GHz the spectrum is more similar to, but slightly wider than, the 17 GHz spectrum.

An FFT of the raw data, i.e. without transforming the data to the local element coordinate system, makes the spectrum fill the whole plot.

4.2 The effects of spatial filtering

Figure 26 illustrates the effect of spatial filtering and shows patterns for element 21 in the smoothly curved array (close to the center of the array) at 17 GHz as raw data and when "gating" the data by removing all spectral points below -50 dB in Figure 23 (points outside the green area), below -40 dB (points outside the yellow area) and by limiting the mode number, $N = \sqrt{N_\theta^2 + N_\varphi^2}$, to $N = 20$.

Some small and fast ripple due to far off scattering or mechanical vibrations is eliminated by this filtering, the stronger the filtering the smaller the ripple. There is still a clear asymmetry in the plots in that there is a bump on the left side (away from the patch feeding probe).

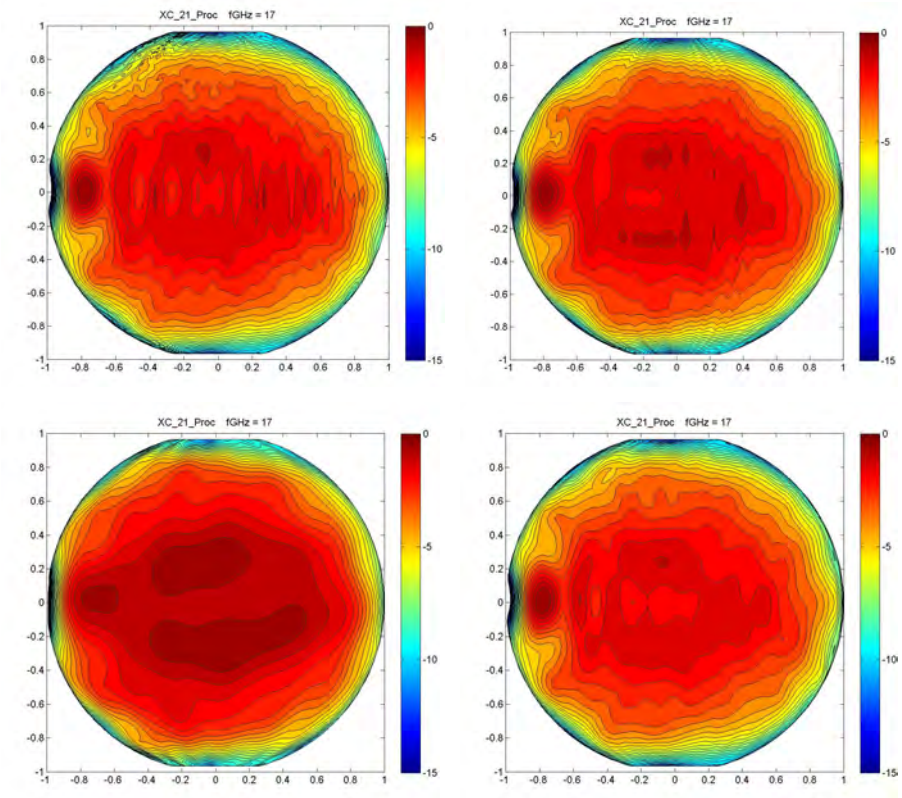

Figure 26 Measured, normalized, φ-polarized element pattern at 17 GHz for element 21. Raw data (upper left), gated at -50 dB (upper right), gated at -40 dB (lower left) and gated at $N = 20$ (lower right). The axes are direction cosines, $v = \sin\theta \sin\varphi$ and $w = \cos\theta$.

This effect is frequency dependent as illustrated in Figure 27 which shows the raw data pattern at 16, 16.5, 17.5 and 18 GHz. At 16 GHz this asymmetrical bump is not visible, (though there is another wave-like ripple) but the asymmetry gets larger as the frequency increases. It should be noted that the array is not very well matched at 16 and 18 GHz, in particular not for wide angle scan. At high frequencies the phase shift between elements for a beam in the bump direction is close to π and we are close to generating a grating lobe (in a planar infinite array). At lower frequencies we are quickly moving away from these conditions and this is probably the reason why the bump disappears so quickly.

Figure 28 shows the cross-polarization power patterns for elements 1 and 21. These patterns are essentially equal, being slightly lower for the edge element.

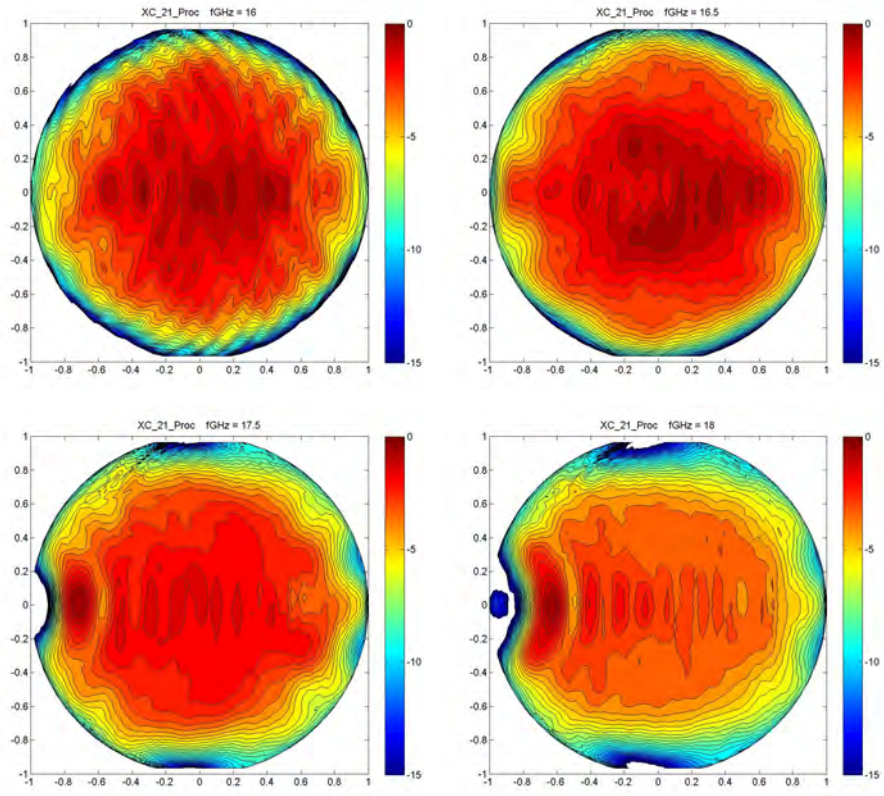

Figure 27 Measured, normalized, φ-polarized element pattern for element 21. At 16 GHz (upper left), 16.5 GHz (upper right), 17.5 GHz (lower left) and 18 GHz (lower right). The axes are direction cosines, $v = \sin\theta\sin\varphi$ and $w = \cos\theta$.

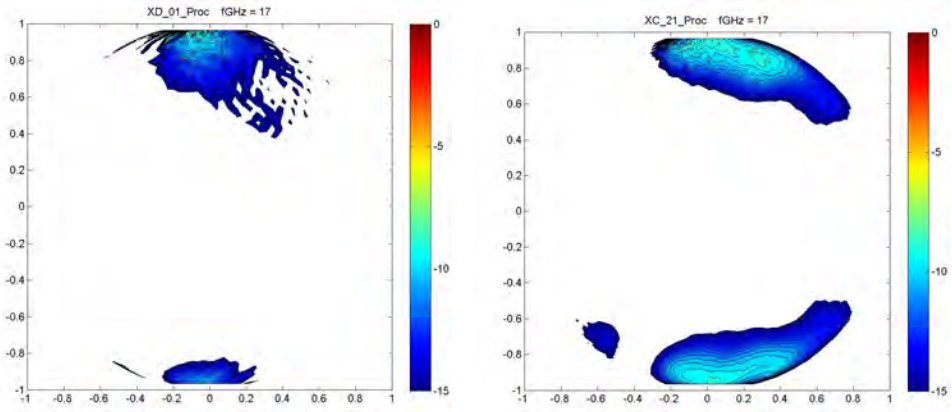

Figure 28 Measured, normalized, θ-polarized element pattern at 17 GHz for elements 1 and 21 in the smoothly curved array. The axes are direction cosines, $v = \sin\theta\sin\varphi$ and $w = \cos\theta$.

Figure 29 shows the co-polarization phase patterns, with reference point in the center of the elements, for the same elements, 1 and 21. The phase patterns are sensitive to the coordinate transformation and for any error in the aligning and mechanical deformation of the mock-up and set up during the measurements. We can here see the same type of asymmetry as in the power patterns.

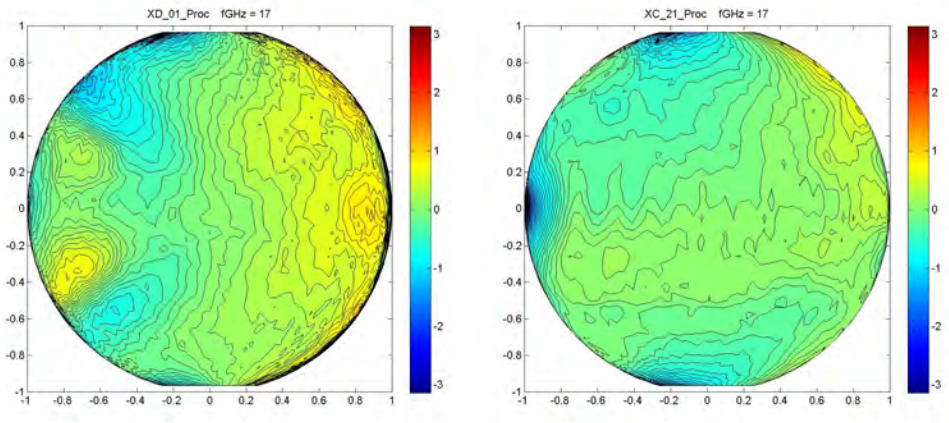

Figure 29 Measured φ-polarized element phase pattern at 17 GHz for elements 1 and 21 in the smoothly curved array. The axes are direction cosines, $v = \sin\theta\sin\varphi$ and $w = \cos\theta$.

4.3 Results for a faceted array

Average patterns, as those for the smooth array in Figure 42 discussed later, can be made here too and are seen in Figure 30 for 17 GHz. One difference between the element patterns in this array and those in the smooth array is that the patterns here will depend on the element position in the subarray and should not be expected to be as equal to each other. If the average is based on center row elements being at least 5 elements from the array end (as for the smooth array) the number of measurements are here limited to 6 (element 22 and 23 for facet position 5, Figure 18, and element 25 – 28 for facet position 4, Figure 21). Due to the reasons discussed above we do not expect these patterns to be as equal as those for the smooth array. These average patterns are very similar to the corresponding plot for the smooth array, the center plot in Figure 42, but the standard deviations of the 6 co-polarization patterns has here an average over all space of -18 to -19 dB, with a maximum of about -10 dB, relative to pattern maximum which is slightly higher than for the smooth array discussed in section 4.4. This corresponds to magnitude and phase variations of 0.7 dB and 5° at the pattern maximum, assuming the errors are equally distributed between them.

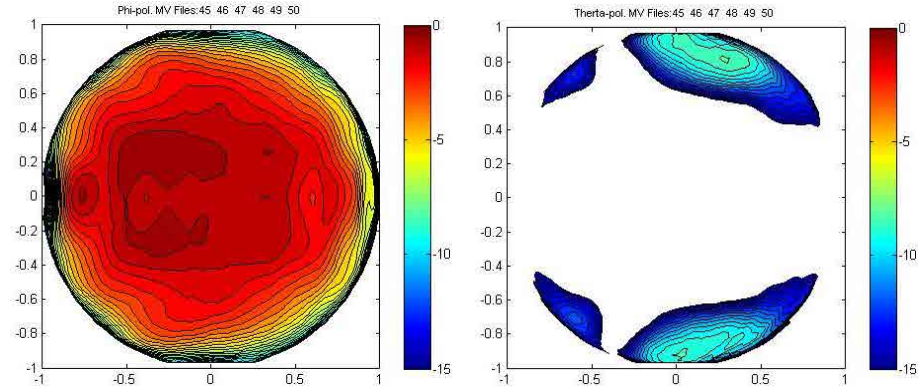

Figure 30 Average of measured element patterns 6–11, i.e. 5 elements or more to array end, at 17 GHz. φ-polarization (left) and θ-polarization (right). The axes are direction cosines, $v = \sin\theta\sin\varphi$ and $w = \cos\theta$.

The patterns may also be compared with the calculated patterns in Figure 13. The calculated array is of course too small to represent the full array but some comparisons can be made. The general behavior is similar to both of the measured arrays except for the edge element where the very strong gain decrease on the left side of the plot is much smaller in the calculated results. The reason for this is yet unclear but the two measured arrays differed mostly here and the actual design of the attachment to ground may be the reason.

4.3.1 Selected patterns

Figure 31 to Figure 41 below shows a selection of various contour plots of for various element patterns. The magnitude plots are normalized to its maximum, co-polarization value, set to 0 dB and the phase patterns are normalized to 0° at element broadside, $(\theta,\varphi)=(0,0)$. The axes of the plots are the direction cosines along the y and z axes, $v=\sin\theta\sin\varphi$ and $w=\cos\theta$. Some elements are measured slightly beyond 90° from broadside but this is not seen in these plots.

In a few measurements there is a small magnitude step at one elevation. It is most clearly seen is in the last plot in Figure 33, for element 4, where a 1 dB step is seen at $\cos\theta\approx 0.6$, $\theta\approx 37°$. It is not seen in the corresponding phase plot in Figure 35 nor is it seen for the other element measured simultaneously (no 47, not shown here). It is probably caused by a cable bend, a connector or a rotational joint and it is not much we can do about it here.

Figure 31 shows co-polarization (along $\hat{\varphi}$) magnitude of 11, consecutive, elements on the center line, for subarray position 4 and 5 in Figure 4, and Figure 32 the same component with the subarray in position 5 and rotated 180°, emulating an un-rotated subarray in position 1 (for practical reasons and since the surrounding of position 1 is different the subarray was not actually measured in that position).

Figure 33 shows co-polarization (along $\hat{\theta}$) magnitude of the 7 elements on the center line with the subarray in position 5 and rotated 90°.

Figure 34 shows co-polarization (along $\hat{\theta}$) magnitude of 3 elements at the edge of the subarray in position 5, rotated 90°.

Figure 35 shows co-polarization phase of 12 elements, chosen from all of the above patterns, i.e. from different elements, subarray positions and subarray rotations.

Figure 36 shows cross-polarization magnitude patterns of the same 12 elements as Figure 35.

Figure 37 to Figure 41 shows co-polarization magnitude of 5 elements (one element in each plot) for frequencies covering the element bandwidth (16, 16.5, 17, 17.5 and 18 GHz). The elements are at the “outer” edge, in the center and “inner” edge of the un-rotated subarray in Figure 37 to Figure 39, an element at the outer edge of the 180° rotated subarray in Figure 40 and an element in the outer edge of the vertically polarized (90° rotated) subarray in Figure 41.

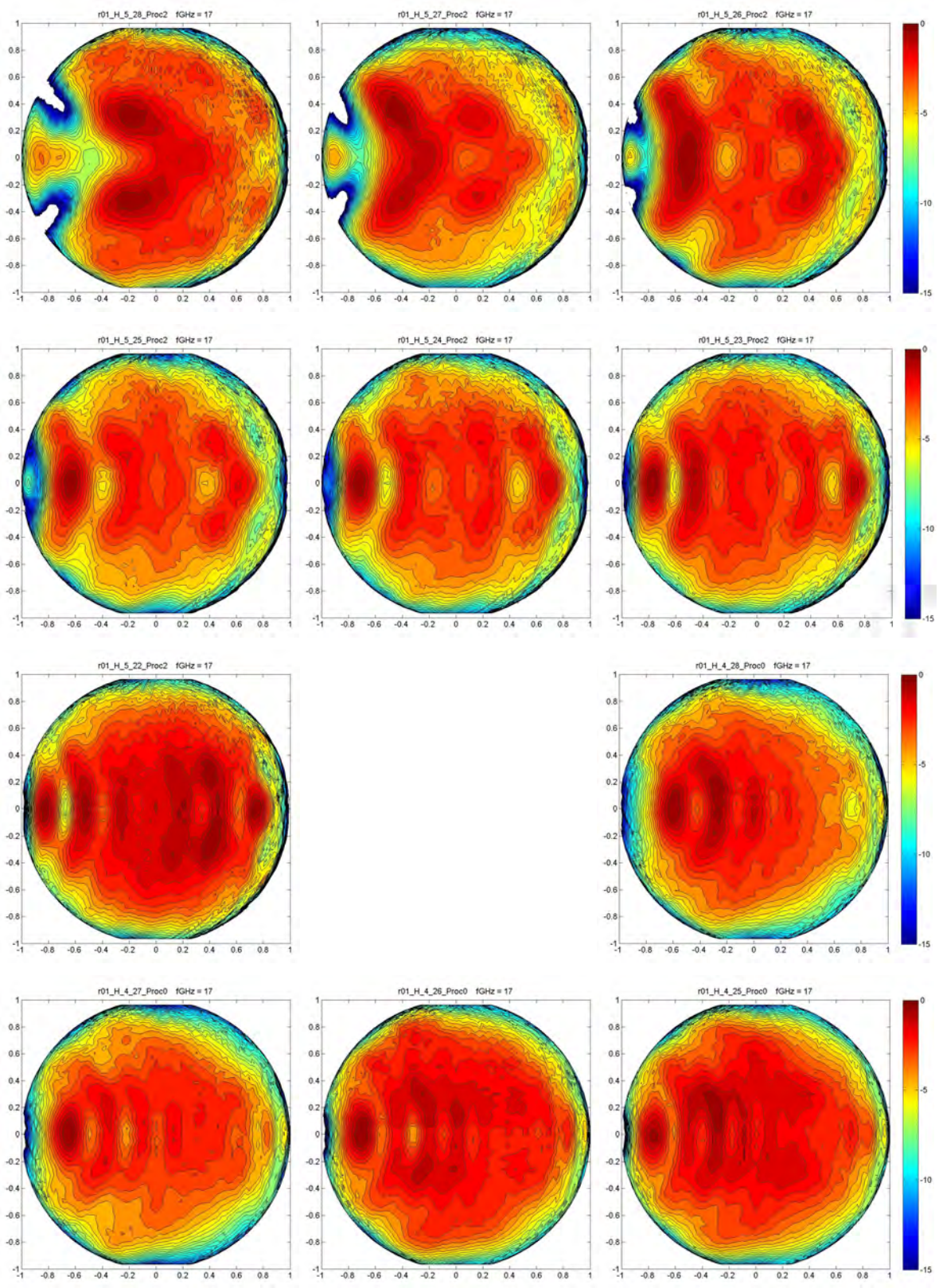

Figure 31 Measured, normalized, φ-polarized element patterns at 17 GHz for the 11 first elements (7 in subarray position 5 and 4 in subarray position 4) in the center row of the faceted array. See Figure 18.

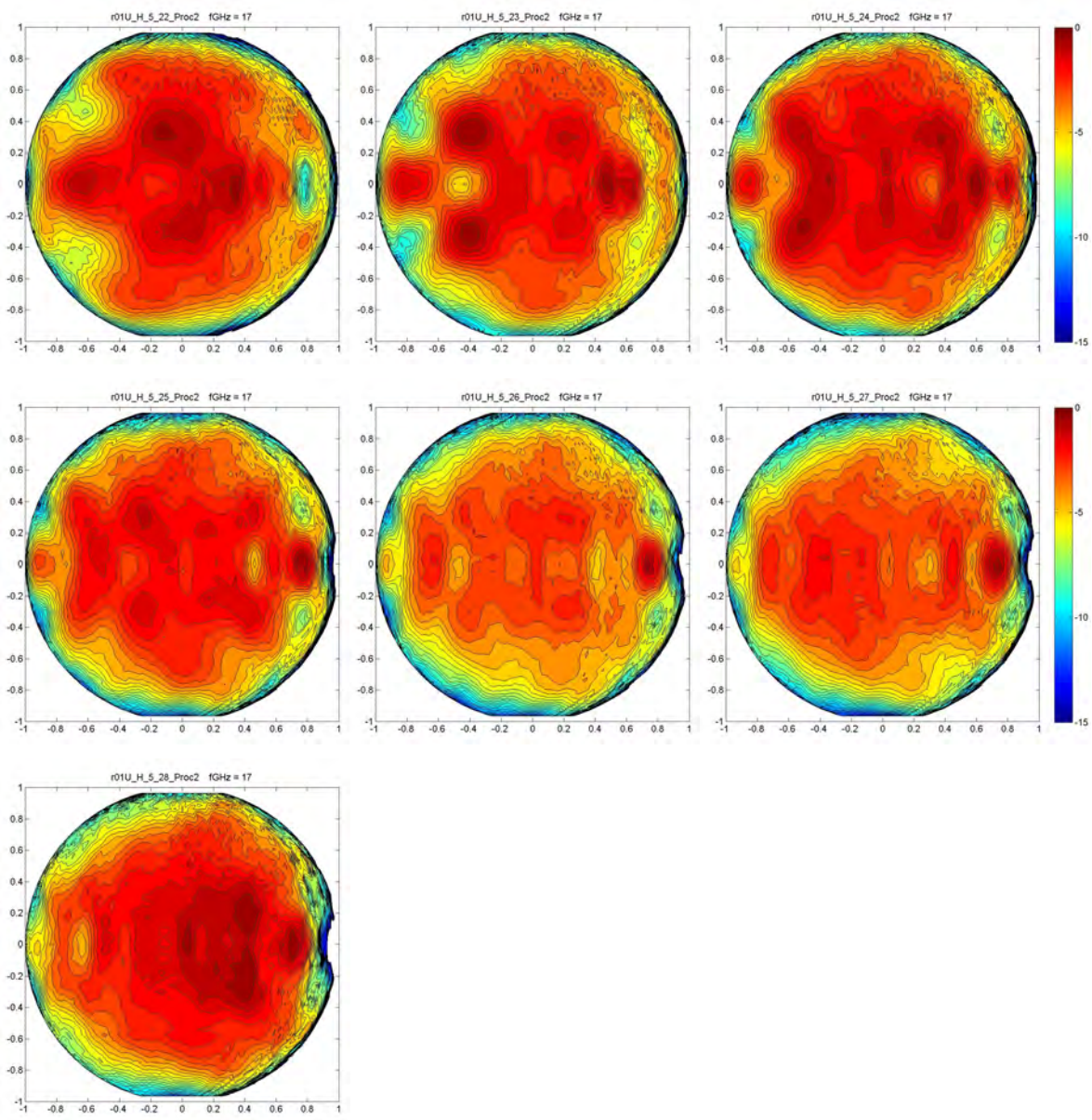

Figure 32 Measured, normalized, φ-polarized element patterns at 17 GHz for the 7 first elements of the upside-down array, in subarray position 5, (emulating 7 elements in the other end of the array) in the center row of the faceted array. See Figure 20.

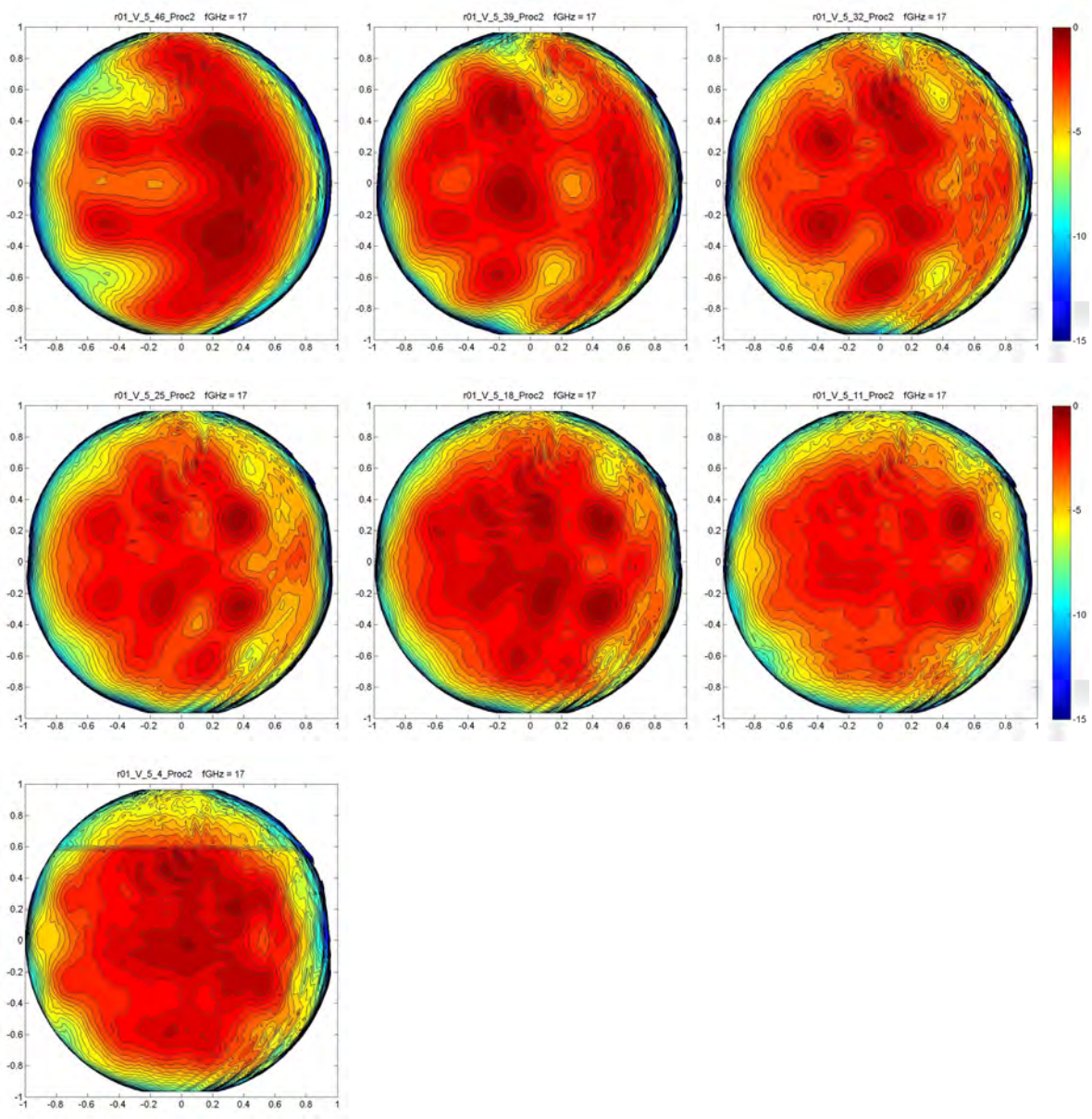

Figure 33 Measured, normalized, θ-polarized element patterns at 17 GHz for the 7 first elements of the vertically polarized array, in subarray position 5, in the center row of the faceted array. See Figure 19.

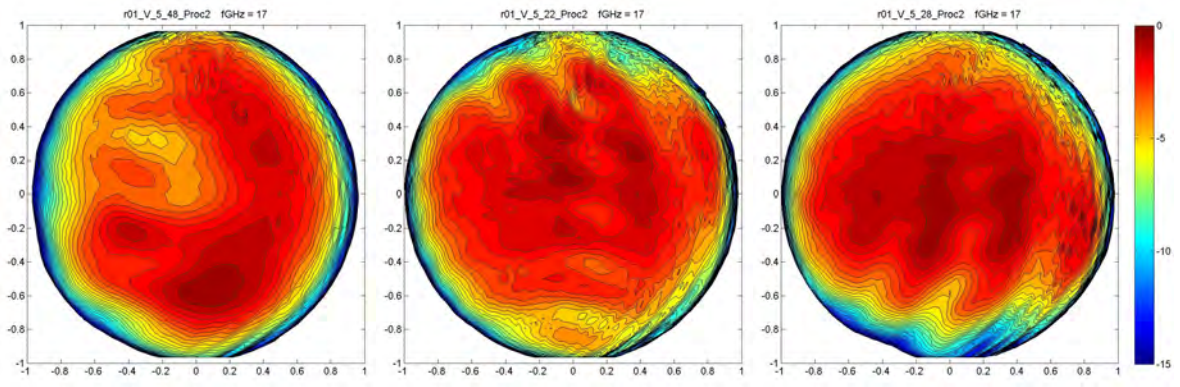

Figure 34 Measured, normalized, θ-polarized element patterns at 17 GHz for 3 elements of the vertically polarized array, in subarray position 5, at the edge of the faceted array. See Figure 19.

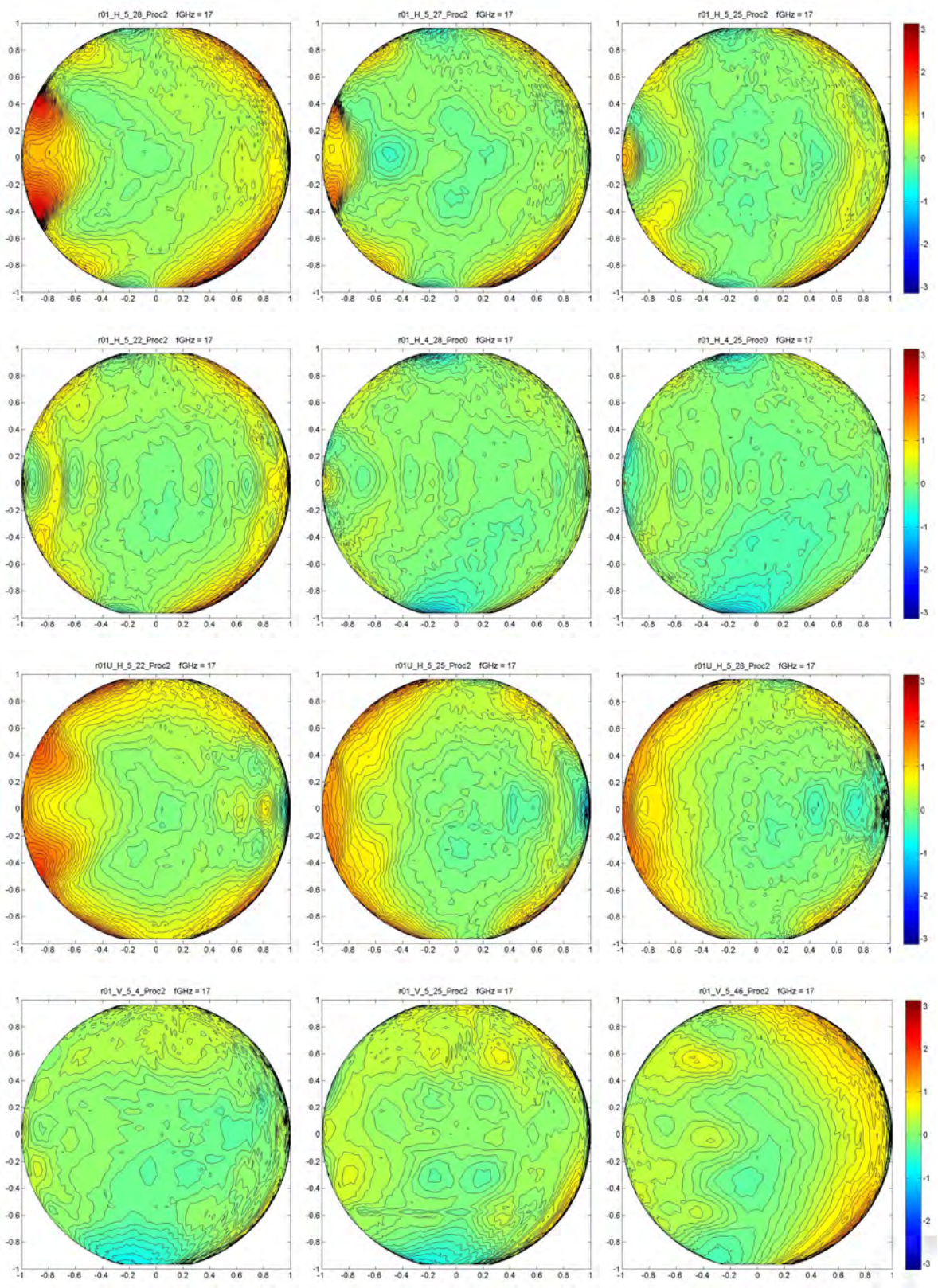

Figure 35 Measured, normalized, co-polarized phase patterns at 17 GHz for various elements.
4 in H-polarized subarray position 5,
2 in H-polarized subarray position 4,
3 in upside-down H-polarized subarray position 5 and
3 in V-polarized subarray position 5
of the faceted array.

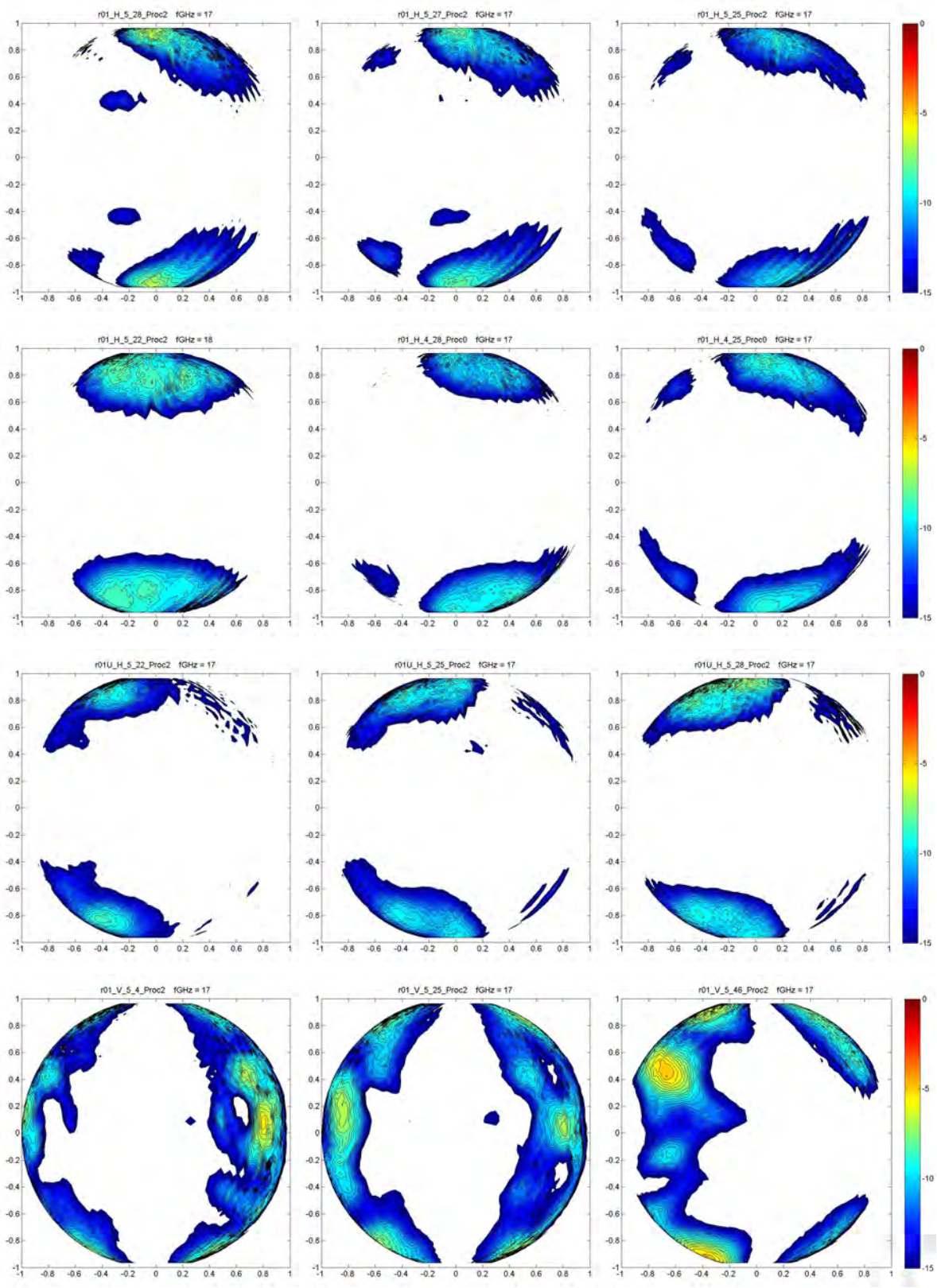

Figure 36 Measured cross polarization patterns, normalization by the co-polarization, at 17 GHz for the same elements as in Figure 35.

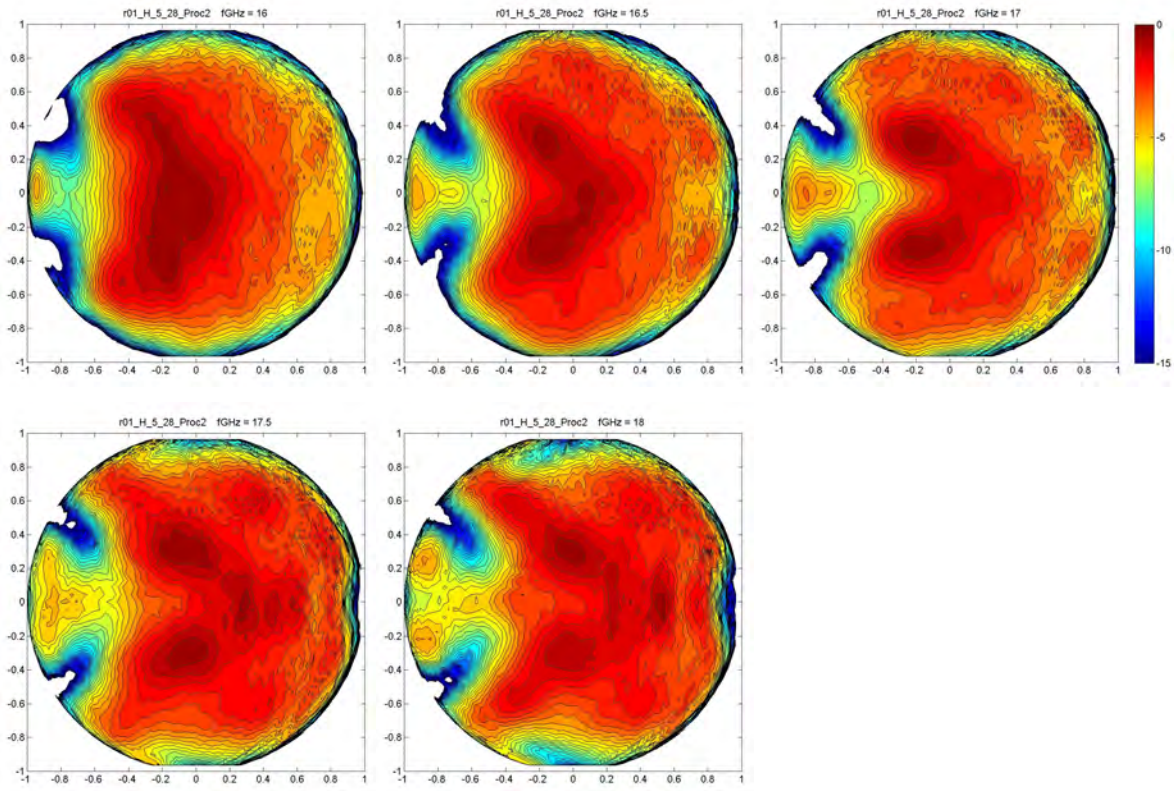

Figure 37 Measured, normalized, φ-polarized element patterns at 16, 16.5, 17, 17.5 and 18 GHz for element 28, at the edge, in subarray position 5. See Figure 18.

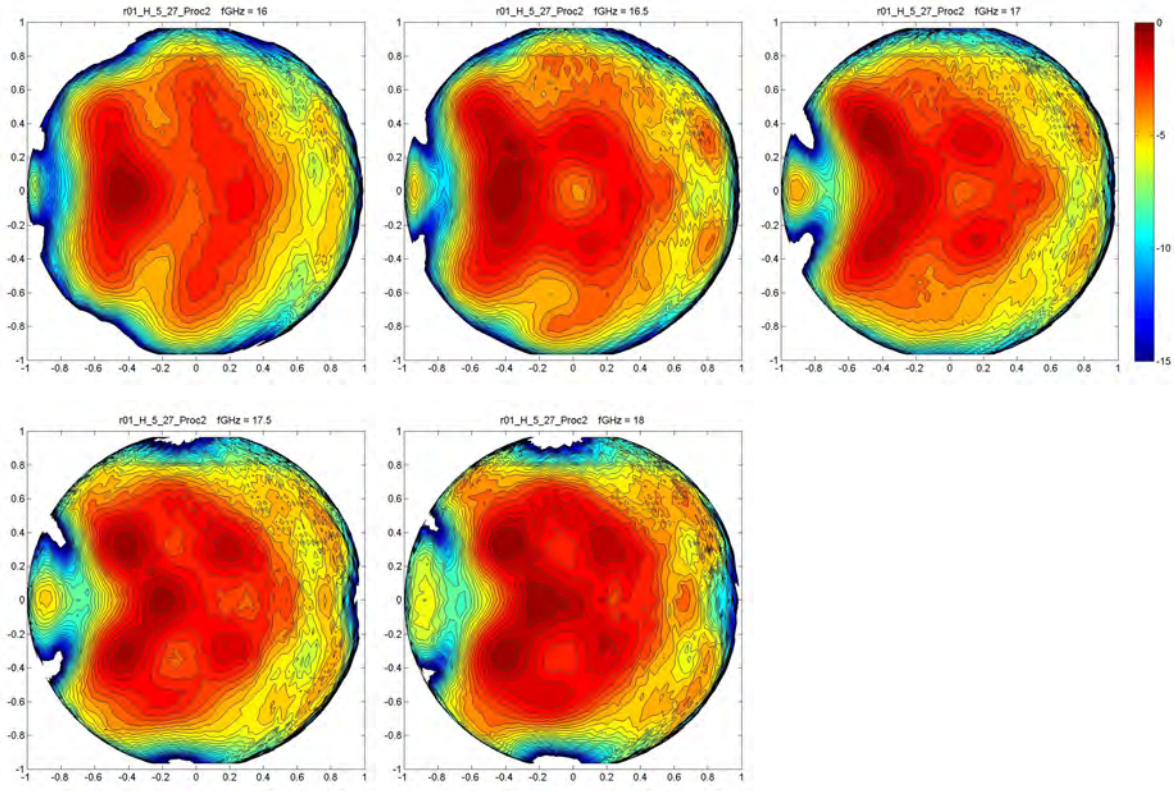

Figure 38 Measured, normalized, φ-polarized element patterns at 16, 16.5, 17, 17.5 and 18 GHz for element 27, next to the edge, in subarray position 5. See Figure 18.

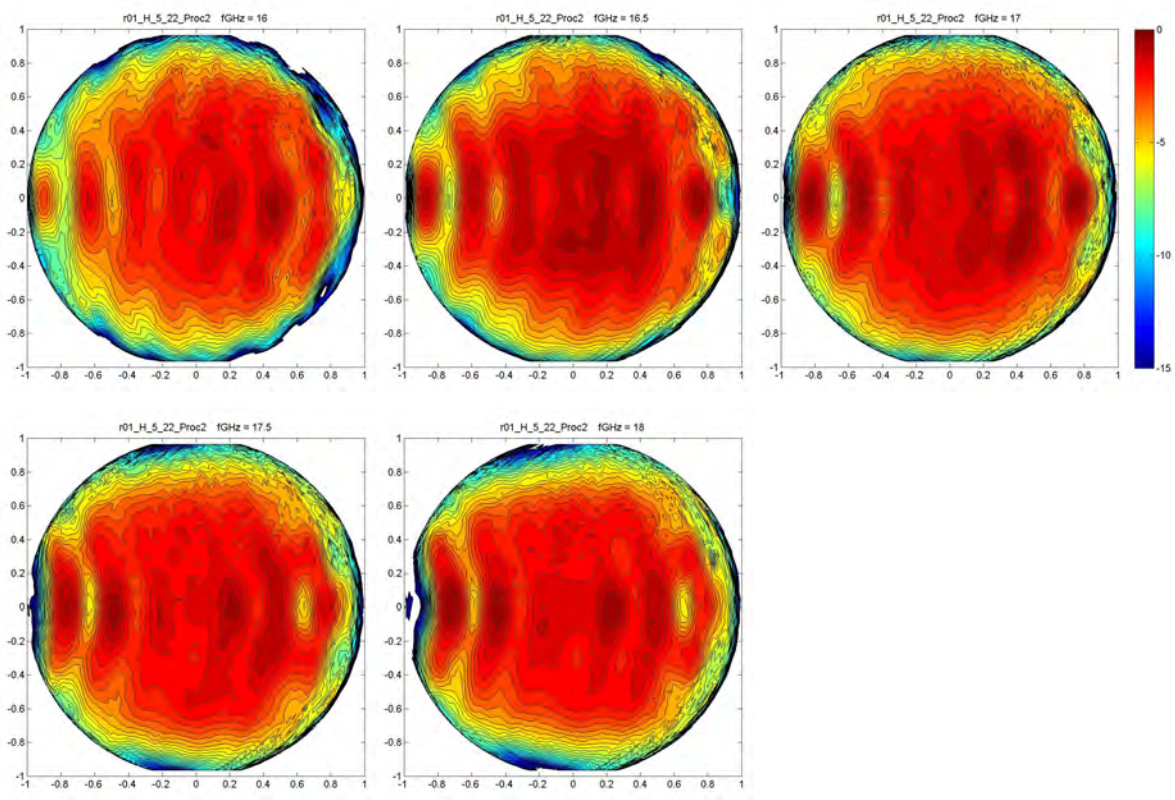

Figure 39 Measured, normalized, φ-polarized element patterns at 16, 16.5, 17, 17.5 and 18 GHz for element 22, farthest away from the edge, in subarray position 5. See Figure 18.

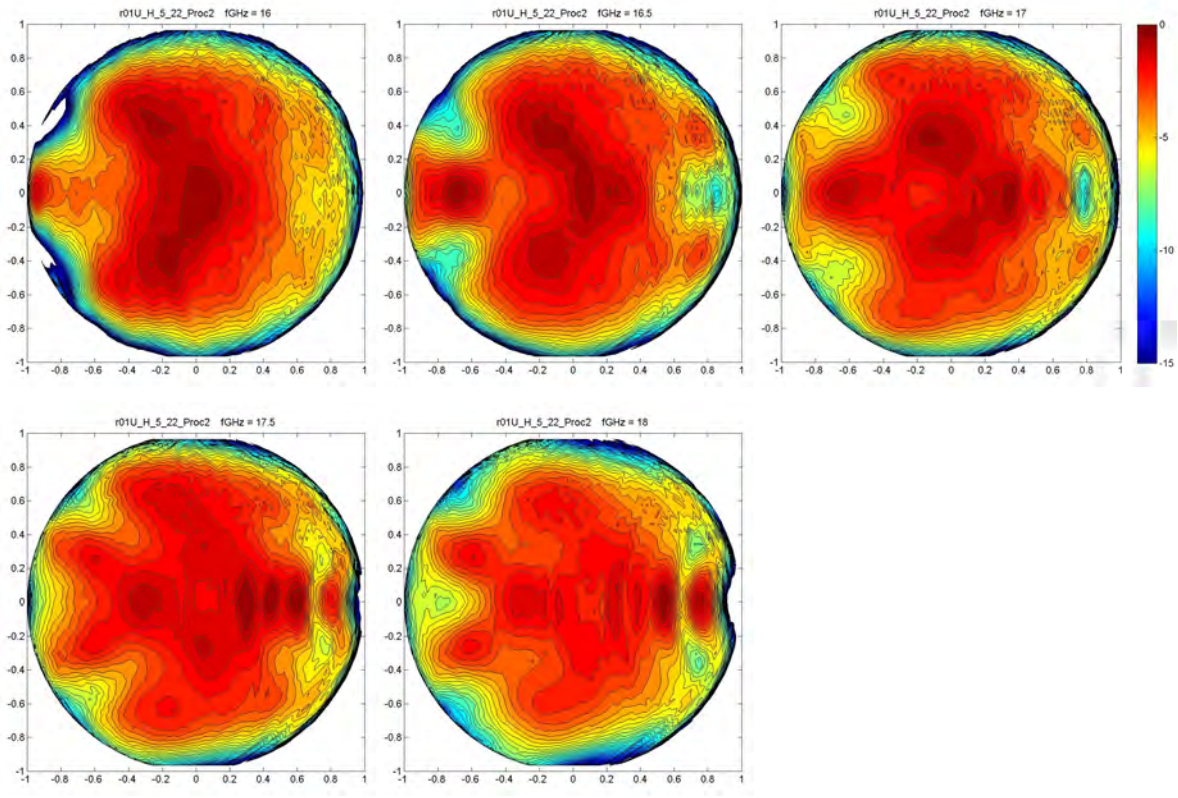

Figure 40 Measured, normalized, φ-polarized element patterns at 16, 16.5, 17, 17.5 and 18 GHz for element 22, at the the edge, in upside-down subarray position 5. See Figure 20.

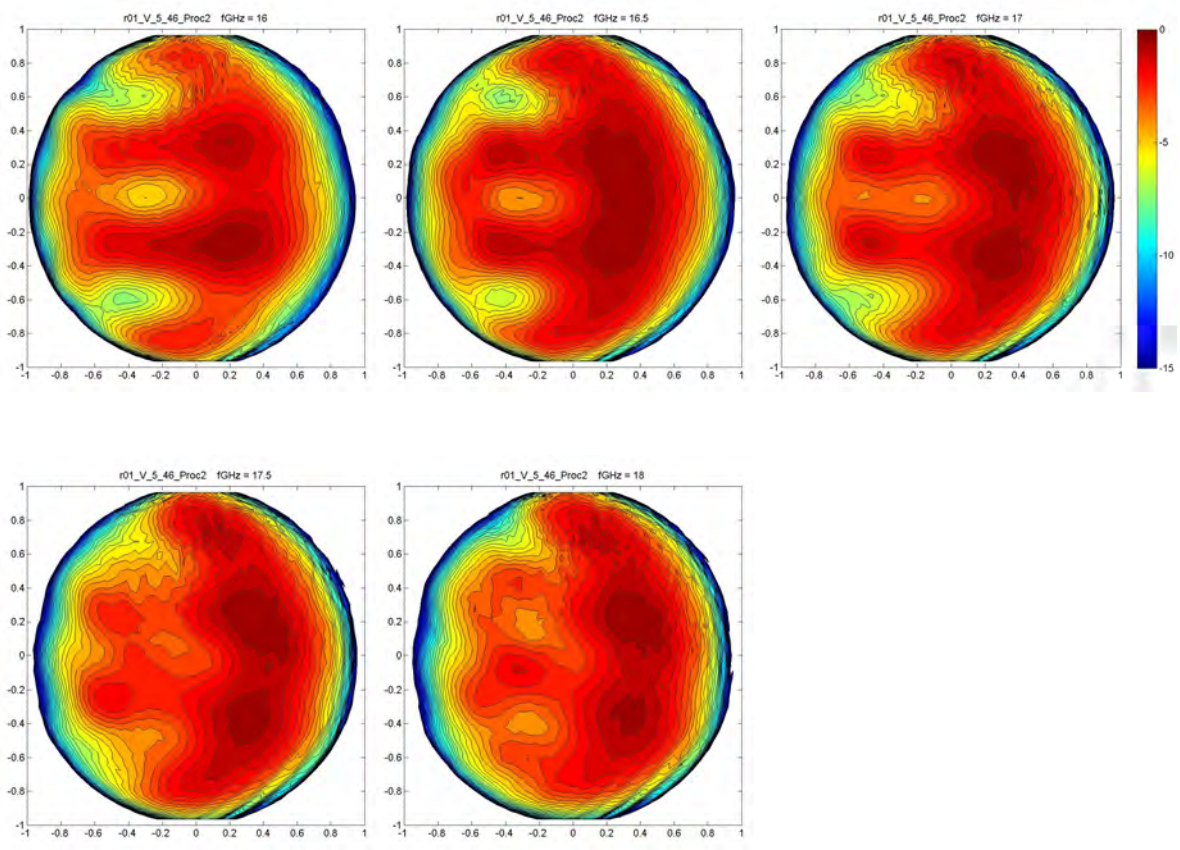

Figure 41 Measured, normalized, θ-polarized element patterns at 16, 16.5, 17, 17.5 and 18 GHz for element 46, at the edge, for vertical polarized subarray in position 5. See Figure 18.

4.4 Results for a smoothly curved array

The element patterns of the "inner" elements of the smooth array, i.e. those far away from the array ends, where the array is circular should ideally be identical in both amplitude and phase. The real elements are not identical however and don't have identical environments. The matching for each of the elements that are never measured consists of a chip resistor with their potential problems and the others have coaxial terminations. Also the feeding of the elements may be sensitive to mechanical tolerances. These variations are analysed by taking the mean value and standard deviation of the 25 complex (magnitude and phase) patterns of elements 6 to 30, i.e. 5 or more elements from the array ends. Figure 42 shows the mean values of the co- and cross-polarization at 16, 17 and 18 GHz. The average patterns of the raw data and of the moderately gated data, as those in Figure 26, gives very similar results since the fast, uncorrelated, ripple in the raw data is removed by the averaging (a -50 dB gate was applied in Figure 42). The standard deviations of the 25 co-polarization patterns had an average over all space of -22 to -23 dB, with a maximum of about -17 dB relative to pattern maximum. This corresponds to magnitude and phase variations of 0.4 dB and 3° at the pattern maximum, assuming the errors are equally distributed between them.

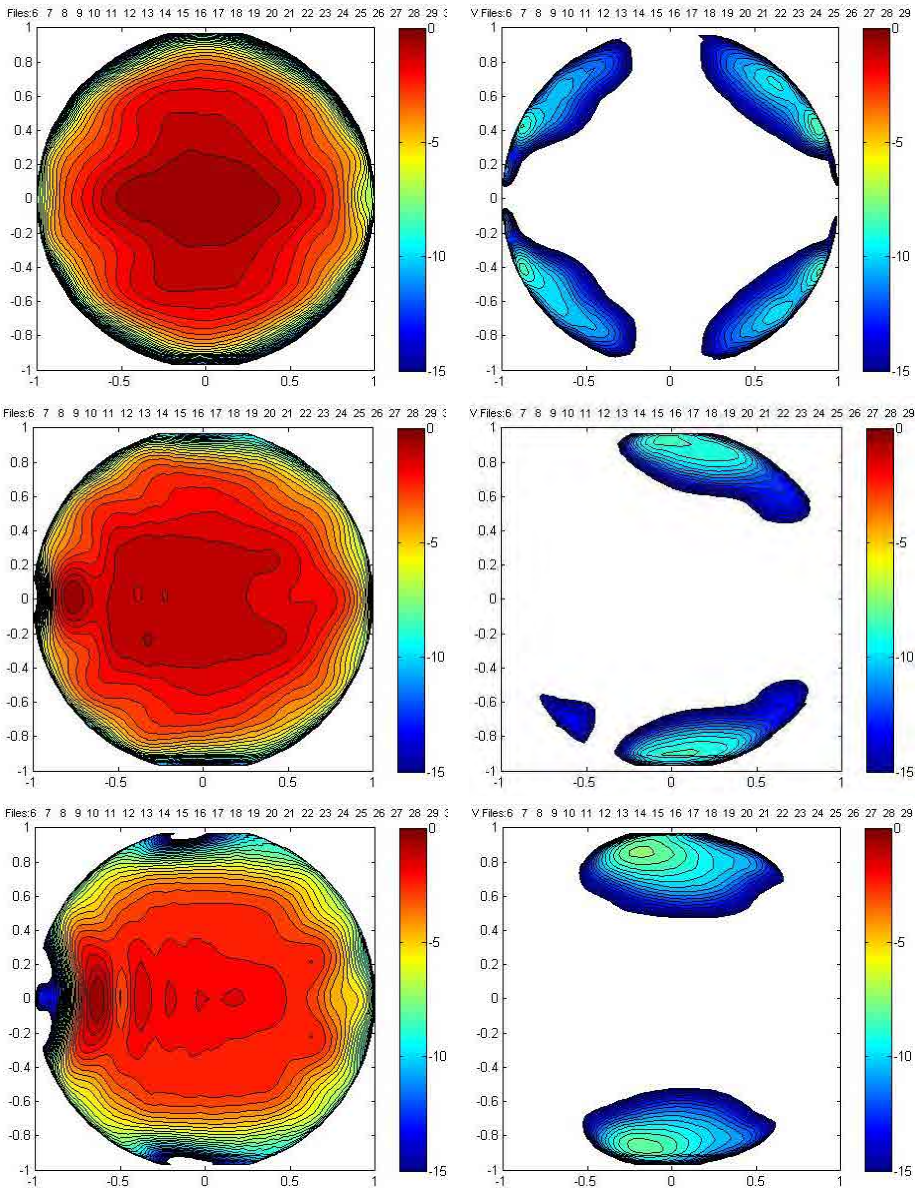

Figure 42 Average of measured element patterns 6–30, i.e. 5 elements or more to array ends, at 16 GHz (upper), 17 GHz (center) and 18 GHz (bottom). A -50 dB "gate", see Figure 23, has been applied. φ-polarization (left) and θ-polarization (right).

This result indicates that if the differences are uncorrelated it would be possible, using the average pattern in the pattern synthesis, to obtain very good pattern quality with low average, error induced, side lobe levels. One may note that since the array elements are pointing in different directions the mutual correlation in a particular global direction will be further decreased.

4.4.1 Selected patterns

Figure 43 to Figure 53 below shows a selection of various contour plots of for various element patterns. The magnitude plots are normalized to its maximum, co-polarization value, set to 0 dB and the phase patterns are normalized to 0° at element broadside, $(\theta, \varphi) = (0, 0)$. The axes of the plots are the direction cosines along the y and z axes, $v = \sin\theta \sin\varphi$ and $w = \cos\theta$. Some elements are measured slightly beyond 90° from broadside but this is not seen in these plots.

Figure 43 shows co-polarization (along $\hat{\varphi}$) magnitudes of all 35 elements on the center line of the array.

Figure 44 shows co-polarization phase of 12 elements, mainly elements close to the ends but also in the center of the array.

Figure 45 shows cross-polarization (along $\hat{\theta}$) magnitude patterns of the same 12 elements as in Figure 44.

Figure 46 shows cross-polarization (along $\hat{\theta}$) phase patterns for 3 elements, at the array ends and center.

Figure 47 to Figure 51 shows co-polarization (along $\hat{\varphi}$) magnitudes of 5 elements (one element in each plot) for frequencies covering the element bandwidth (16, 16.5, 17, 17.5 and 18 GHz). The elements are close to the ends and in the center of the array.

Figure 52 shows cross-polarization (along $\hat{\theta}$) magnitudes of one element (number 18 in the center) for frequencies covering the element bandwidth (16, 16.5, 17, 17.5 and 18 GHz).

Figure 53 shows co-polarization (along $\hat{\varphi}$) phase patterns of one element (number 18 in the center) for frequencies covering the element bandwidth (16, 16.5, 17, 17.5 and 18 GHz).

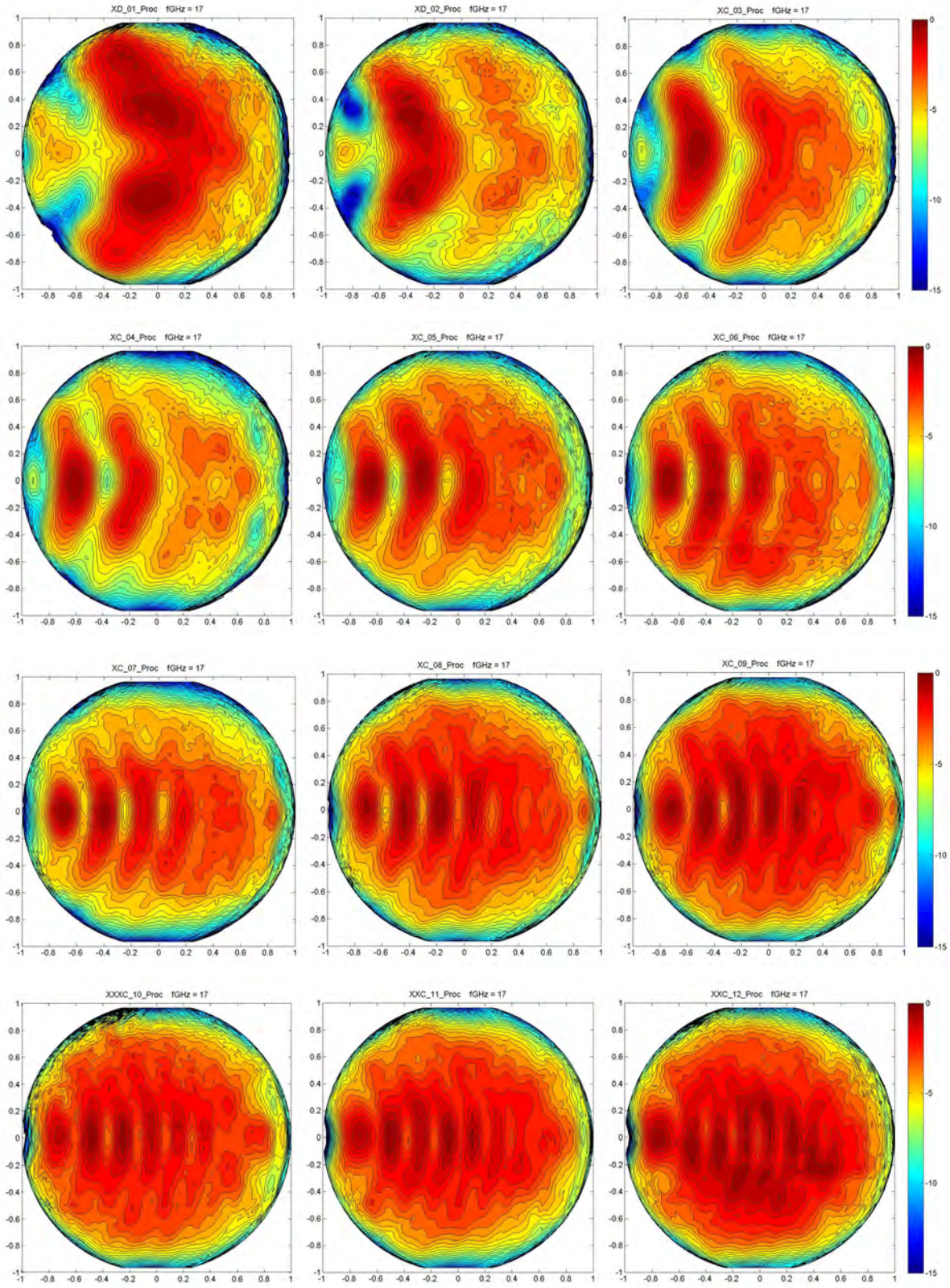

Figure caption see later.

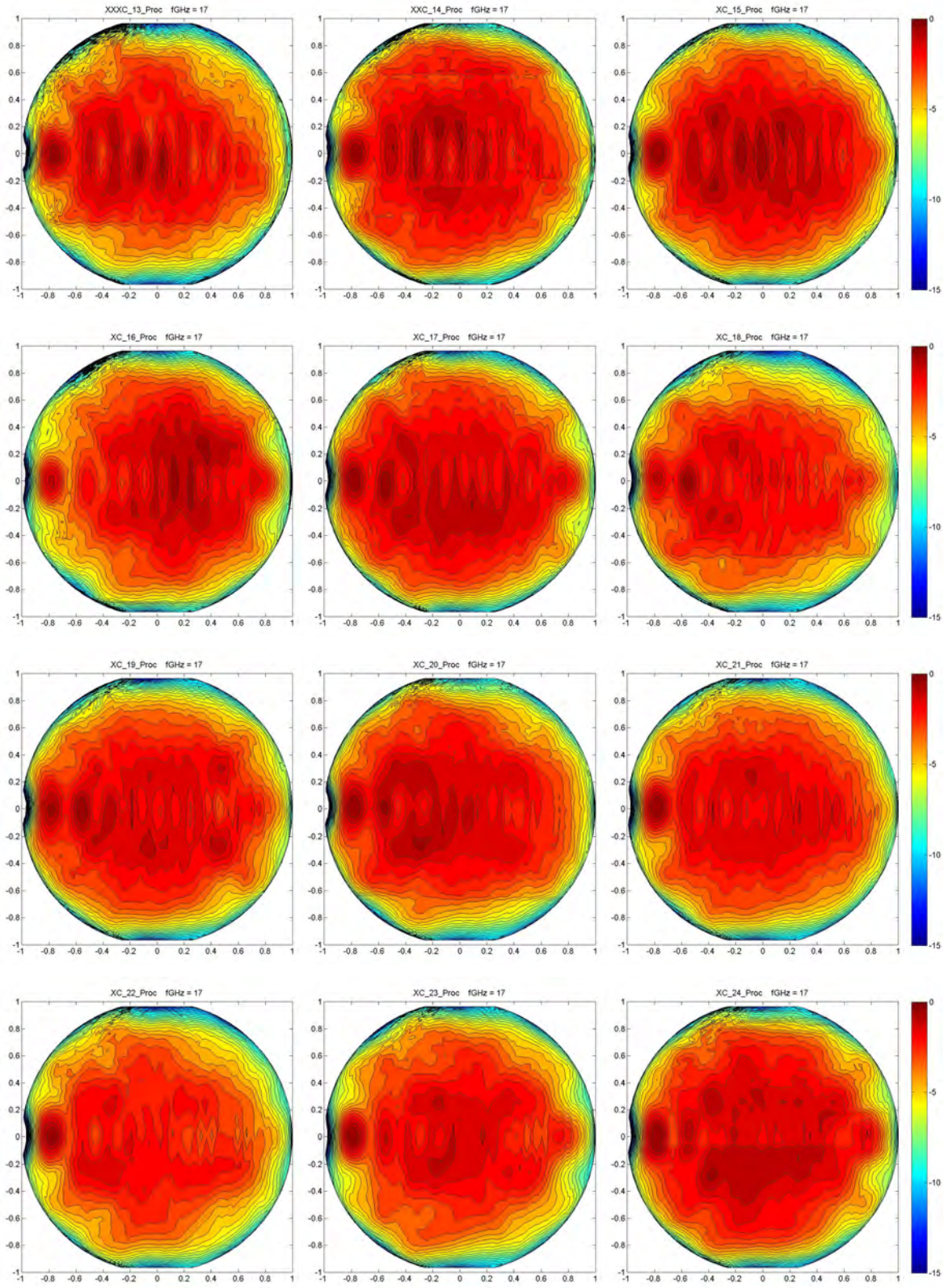

Figure caption see later.

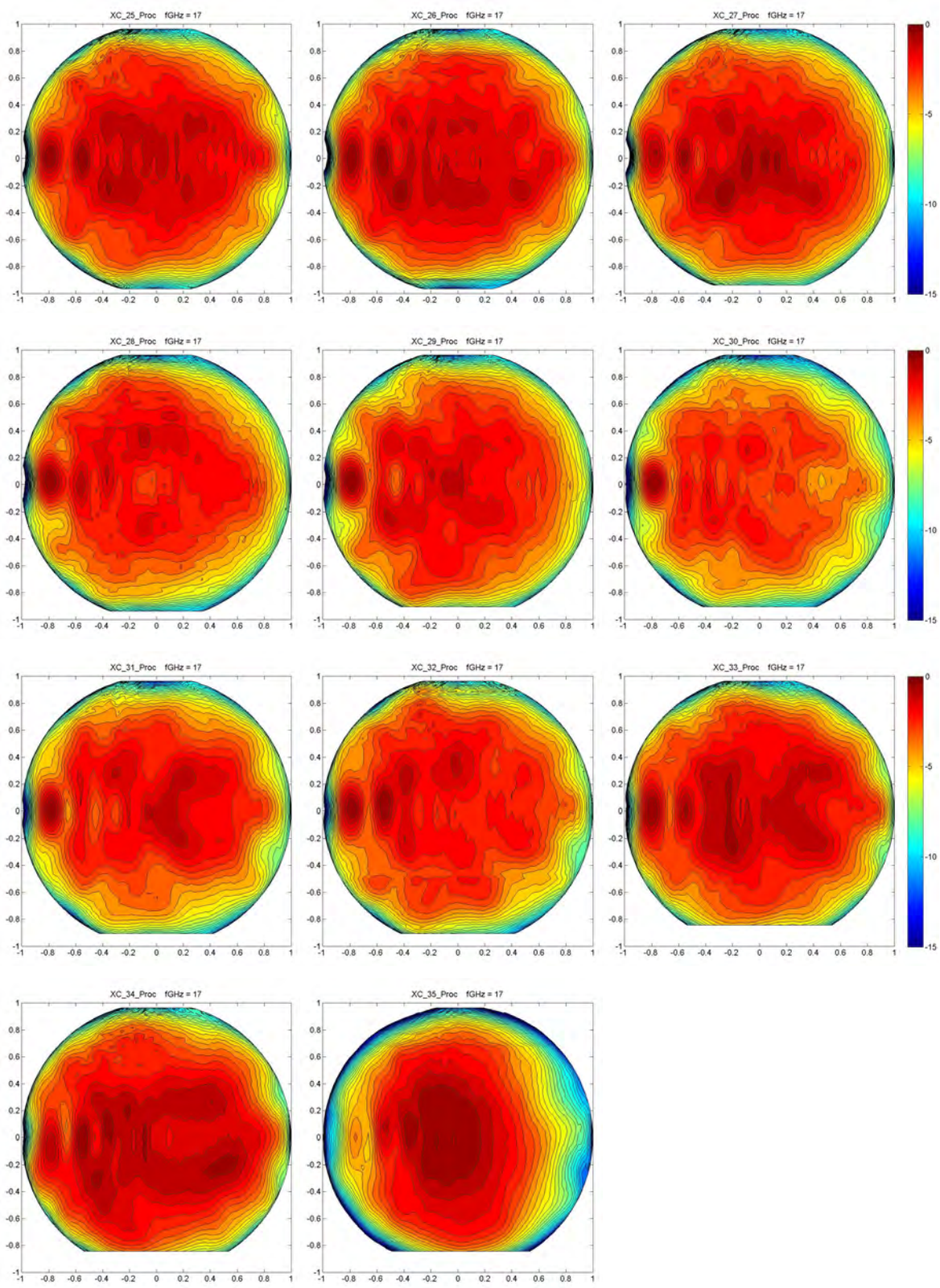

Figure 43 Measured, normalized, φ-polarized element patterns at 17 GHz for all elements in the center row of the smoothly curved array. See Figure 22.

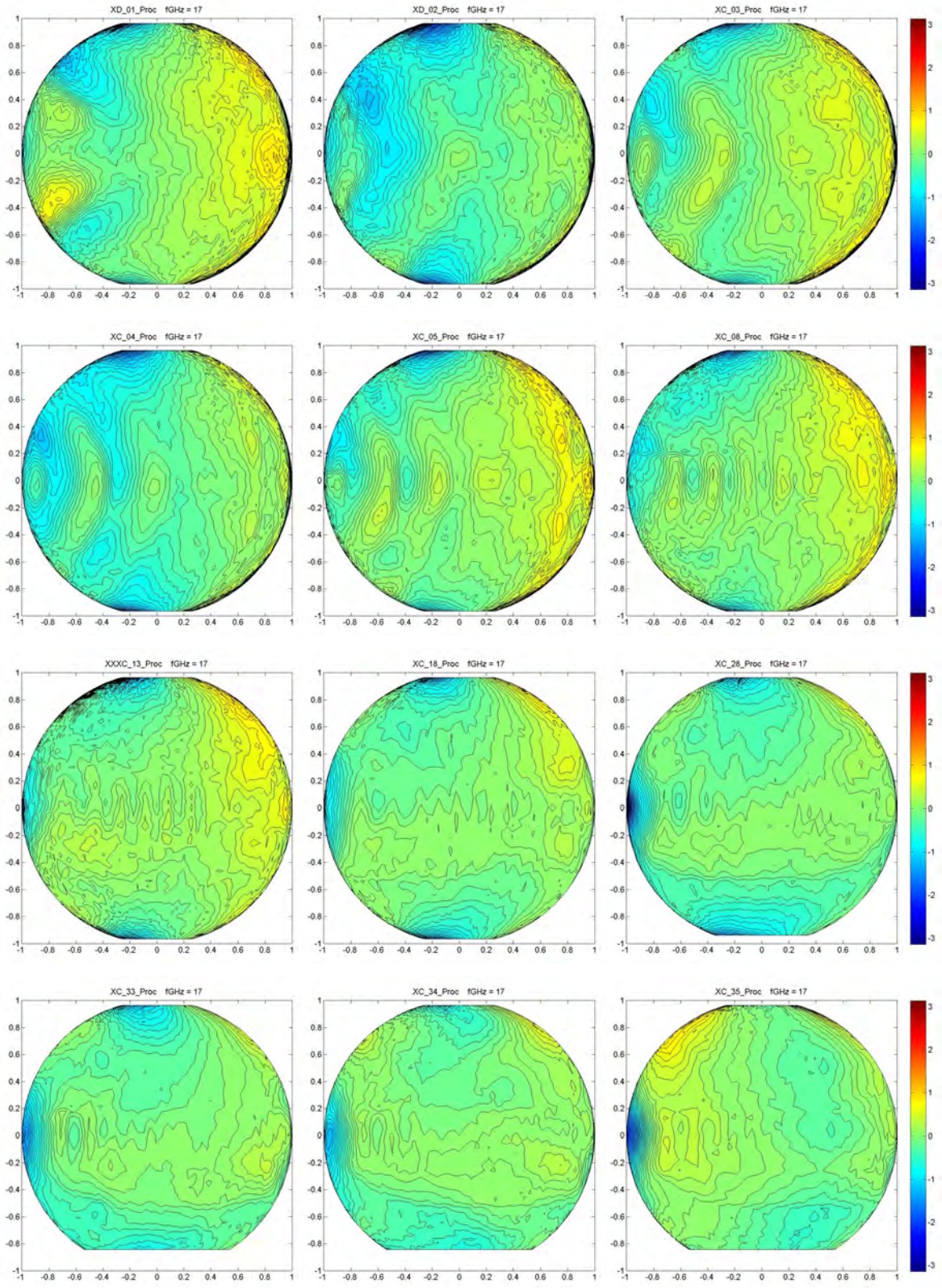

Figure 44 Measured, normalized, φ-polarized phase patterns at 17 GHz for a selection of elements at the two ends and in the center of the smoothly curved array. See Figure 22.

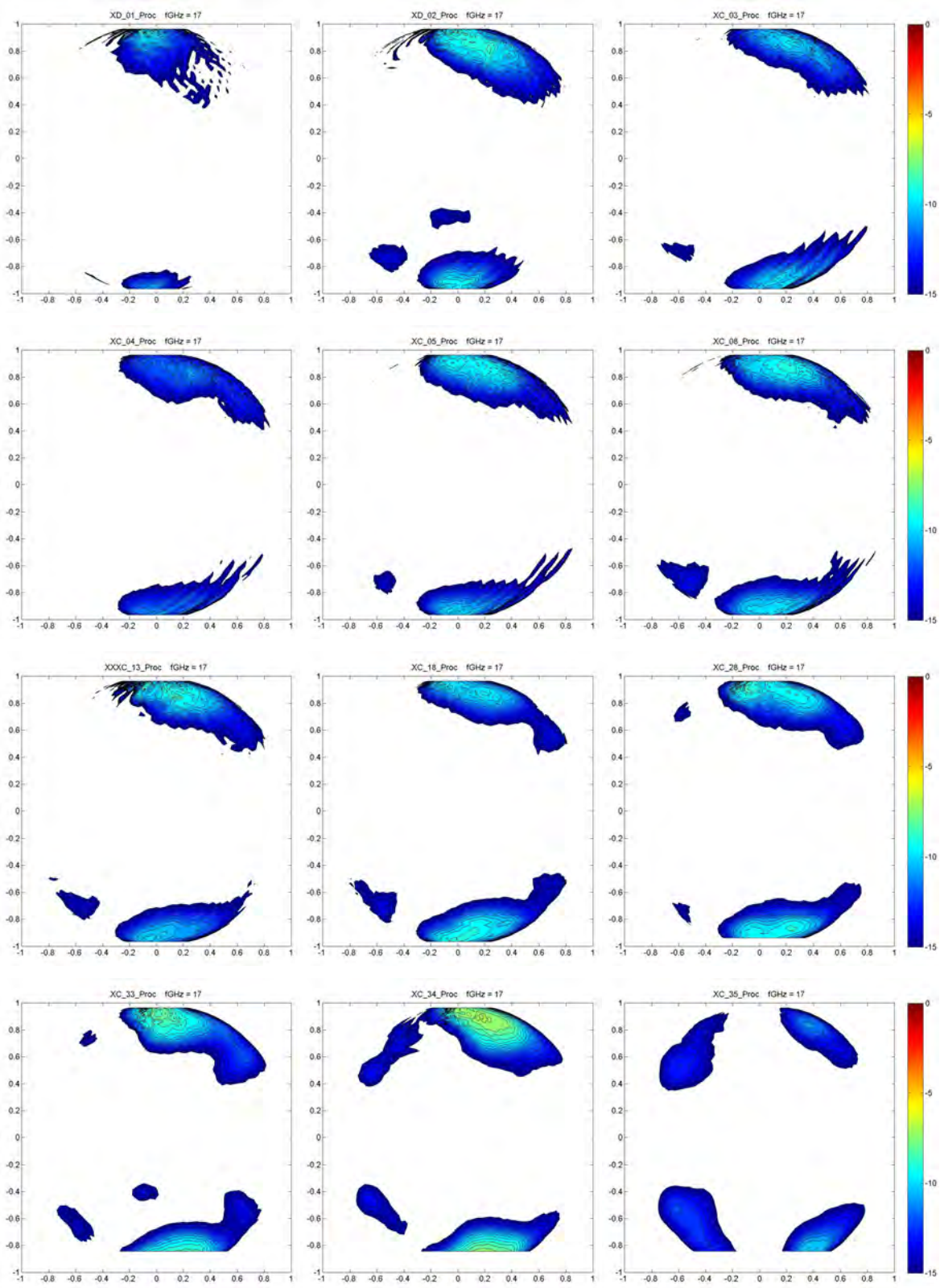

Figure 45 Measured, normalized, cross polarization (θ-polarized) element patterns at 17 GHz for a selection of elements at the two ends and in the center of the smoothly curved array. See Figure 22.

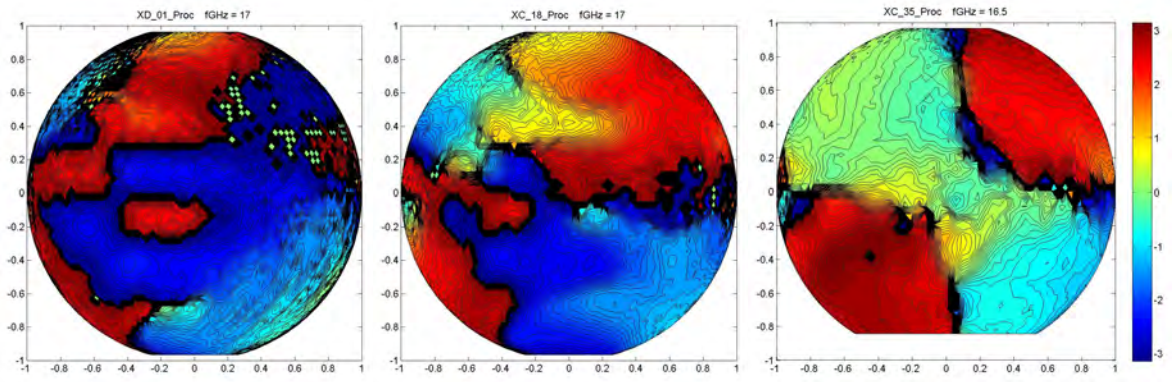

Figure 46 Measured, normalized, phase patterns of the cross polarization at 17 GHz for three elements at the two ends and in the center of the smoothly curved array. See Figure 22.

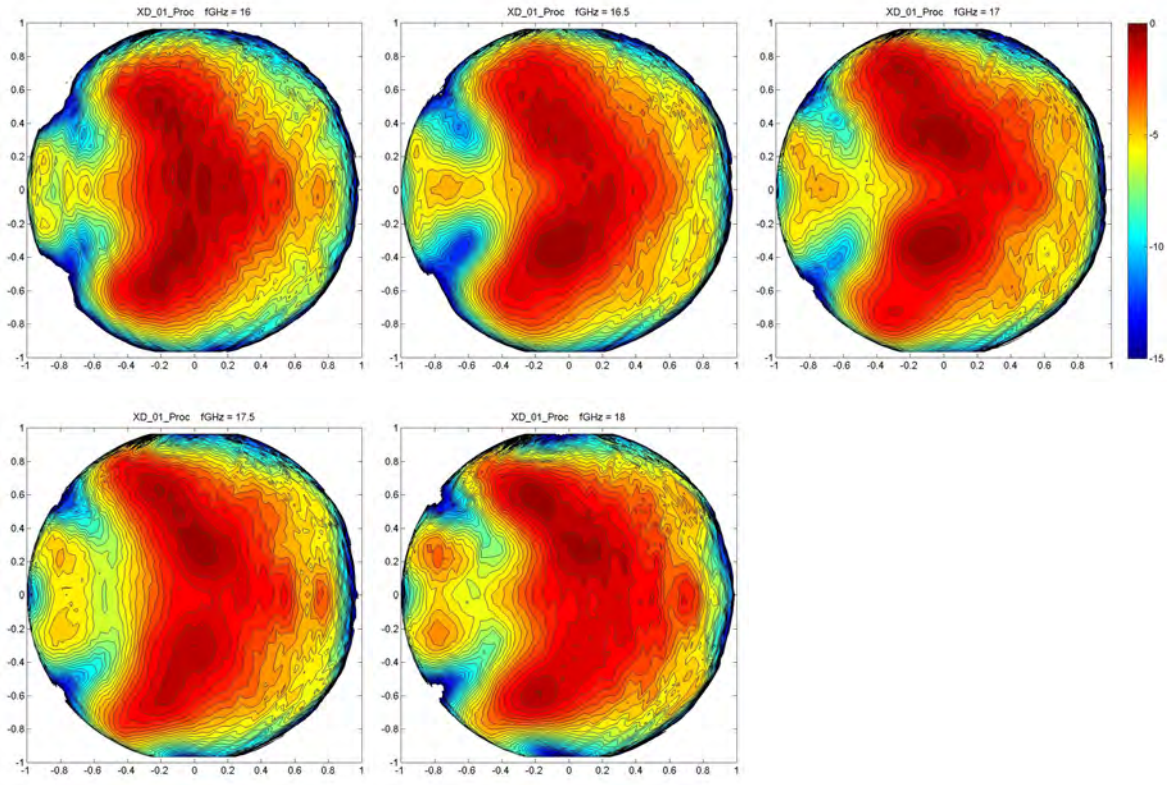

Figure 47 Measured, normalized, φ-polarized element patterns at 16, 16.5, 17, 17.5 and 18 GHz for element 1, at the edge, of the smoothly curved array. See Figure 22.

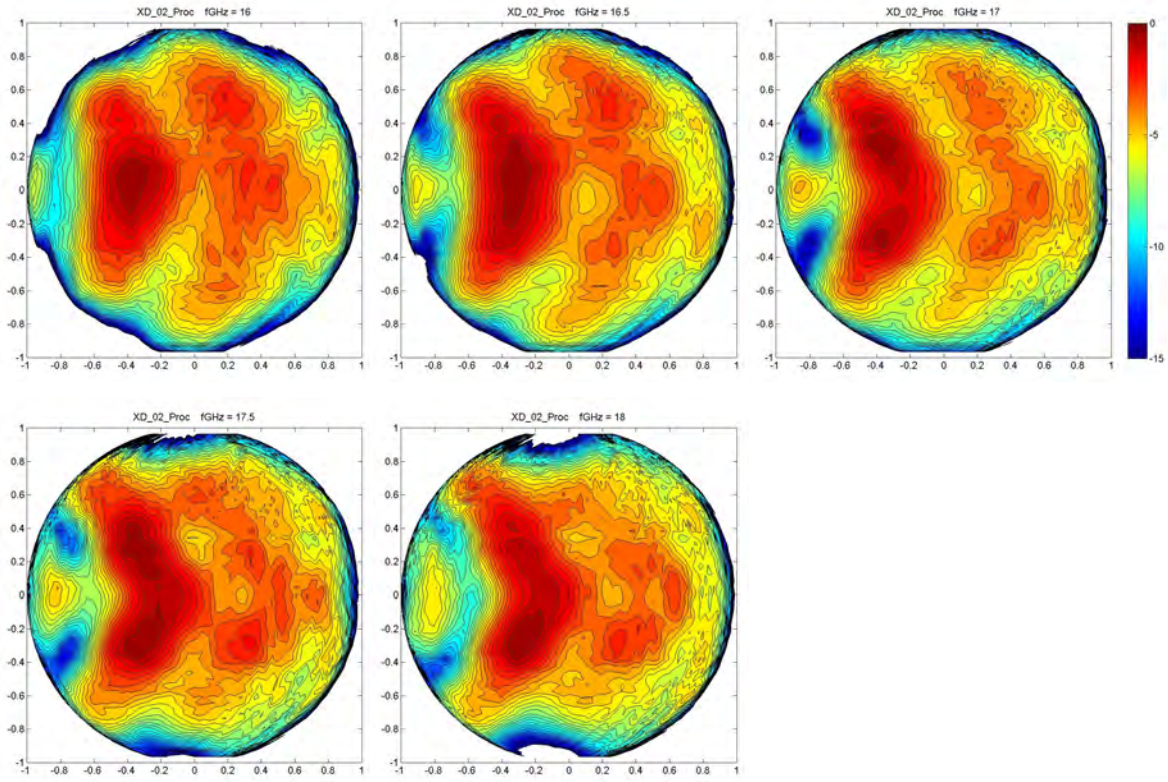

Figure 48 Measured, normalized, φ-polarized element patterns at 16, 16.5, 17, 17.5 and 18 GHz for element 2, close to the edge, of the smoothly curved array. See Figure 22.

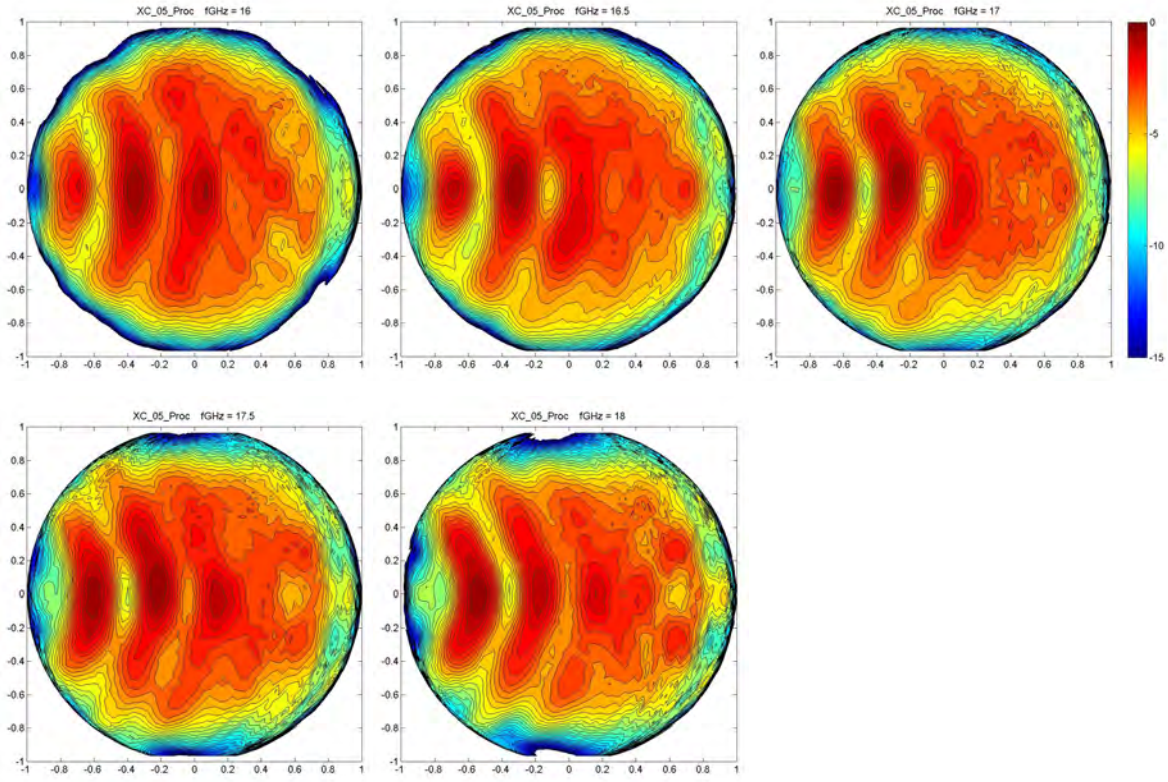

Figure 49 Measured, normalized, φ-polarized element patterns at 16, 16.5, 17, 17.5 and 18 GHz for element 5 of the smoothly curved array. See Figure 22.

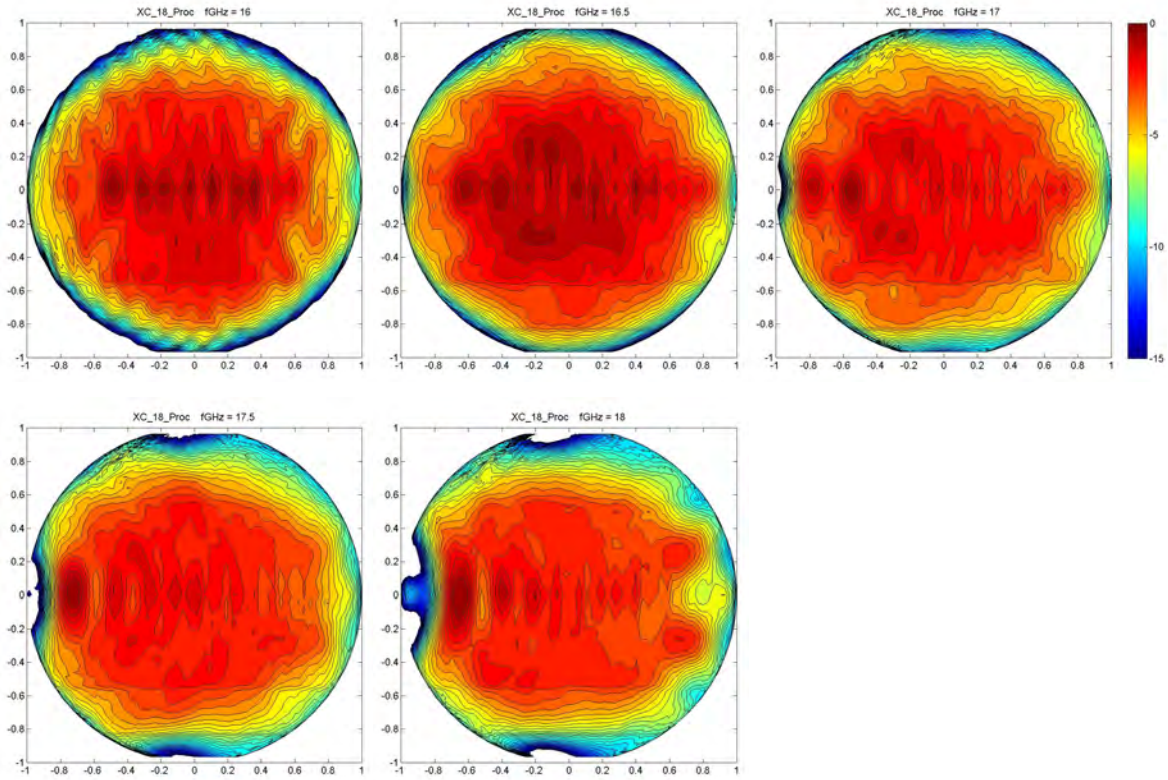

Figure 50 Measured, normalized, φ-polarized element patterns at 16, 16.5, 17, 17.5 and 18 GHz for element 18, in the center of the smoothly curved array. See Figure 22.

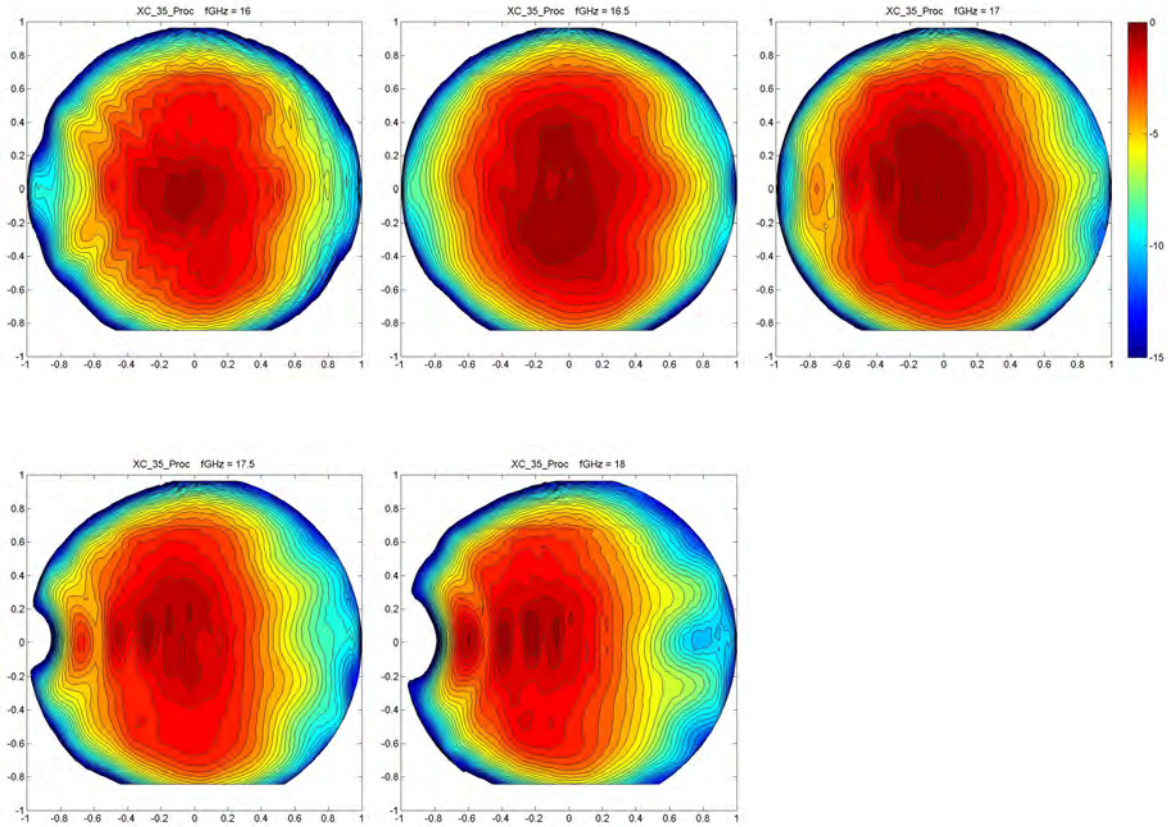

Figure 51 Measured, normalized, φ-polarized element patterns at 16, 16.5, 17, 17.5 and 18 GHz for element 35, at the edge, of the smoothly curved array. See Figure 22.

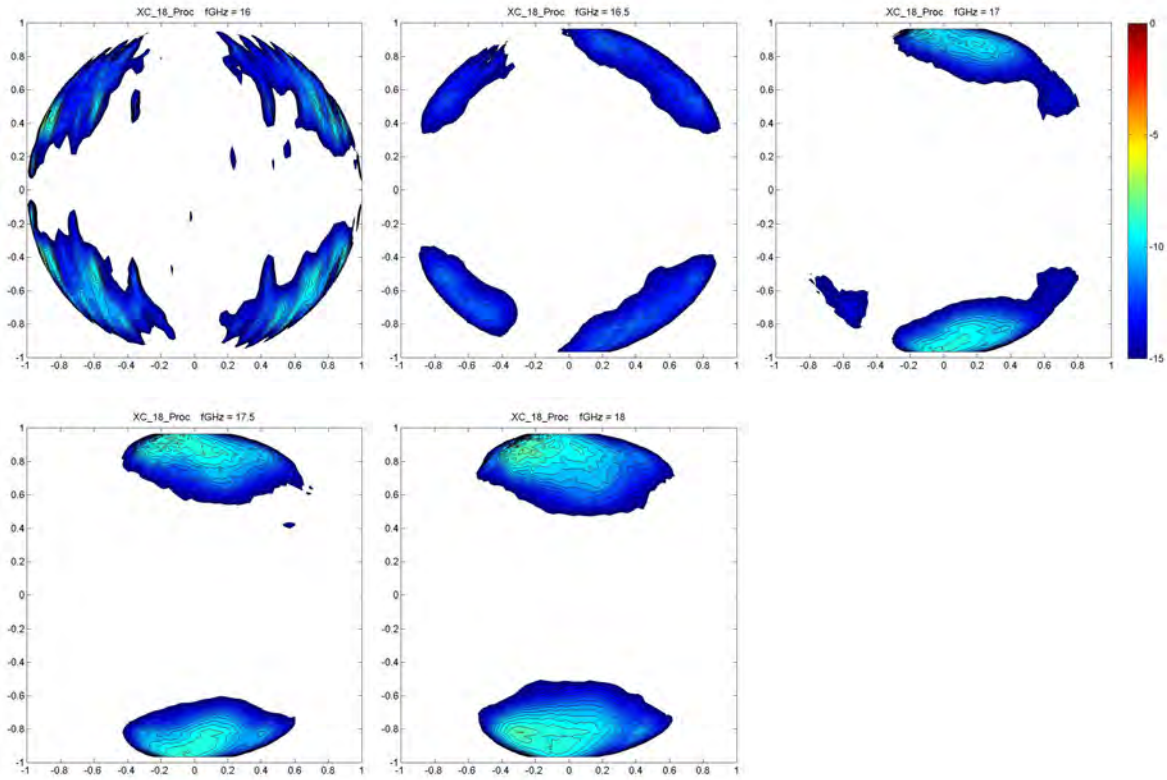

Figure 52 Measured, normalized, cross polarization (θ-polarized) element patterns at 16, 16.5, 17, 17.5 and 18 GHz for element 18 in the center of the smoothly curved array. See Figure 22.

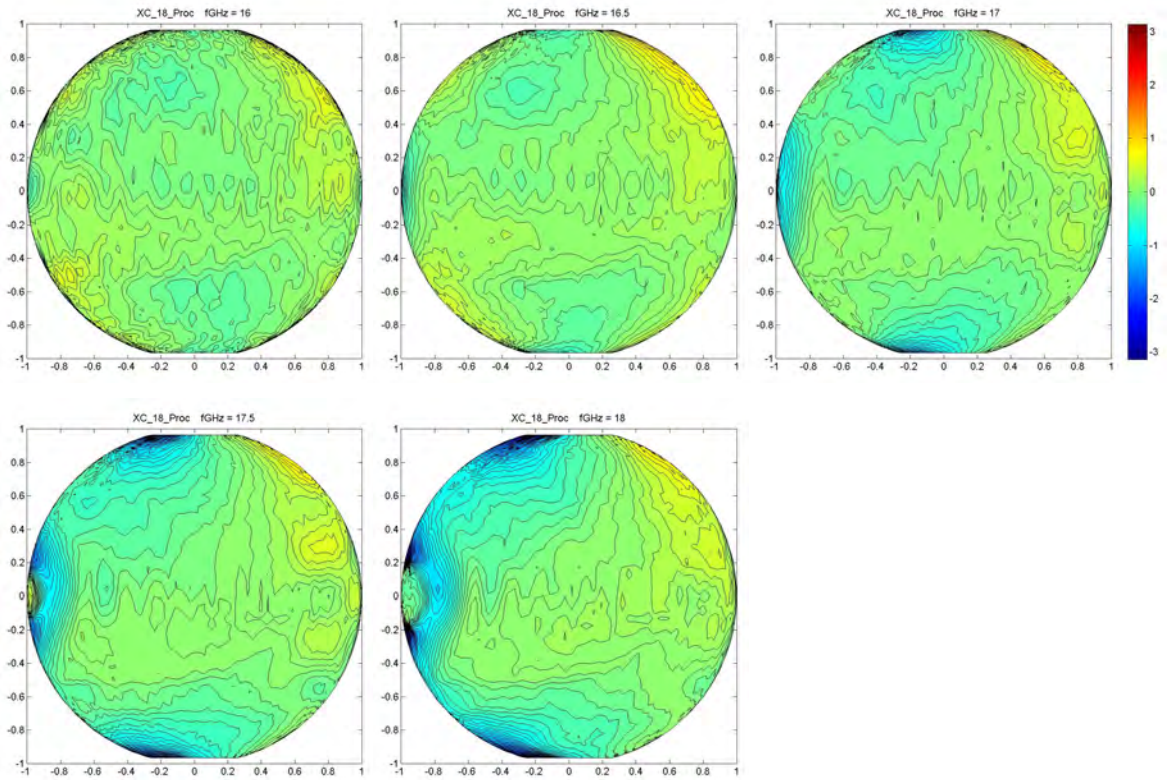

Figure 53 Measured, normalized, φ-polarized phase patterns at 16, 16.5, 17, 17.5 and 18 GHz for element 18 in the center of the smoothly curved array. See Figure 22.

5 Measured patterns in the VISCA simulator

The behavior of a full array antenna beam is simulated with an in-house developed tool, VISCA [4], where its scanning, coverage, cross polarization, and pattern synthesis can be studied, using the measured element patterns to form beams.

A synthesized beam using a maximum gain criterion, i.e. $w_n \propto g^*_{co,n}\left(\theta_{scan},\varphi_{scan}\right)$ so that $G_{co,Array} = \sum_n G_{co,n}$, is shown in Figure 54 for the horizontal plane while Figure 55 shows the same beam in 3D together with the UAV flying over the terrain. The array is a full faceted array with 9 subarrays as depicted in Figure 3 and Figure 4 but, due to the faceted geometry, essentially only 7 subarrays are active which gives an aperture efficiency of about -2 dB. Simulations show that the array exhibit good scanning performance, covering the expected scan range.

Simple tapering of the weights are easily obtained, e.g. by multiplication with a standard smooth taper over the active subarrays. In general of course the beam pattern synthesis is more difficult for conformal arrays.

The ripples in the element patterns are essentially not random but still mainly relatively uncorrelated. All elements have not been measured however but some patterns have been used for several elements, at appropriate positions and with a change of symmetry where required. This will tend to correlate the elements and thus, for example, increase the error induced sidelobes.

Totally uncorrelated RMS variations of 1 dB and 10º (± two steps in the contour plots in section 4.3) and using 7 subarrays would give RMS error induced sidelobes of about -37 dB relative to the beam peak, while the -18 dB standard deviations in section 4.3 (obtained by only using six “central elements) would give -41 dB. The error induced (far out) sidelobes of the pattern in Figure 54 can be estimated to about -35 dB.

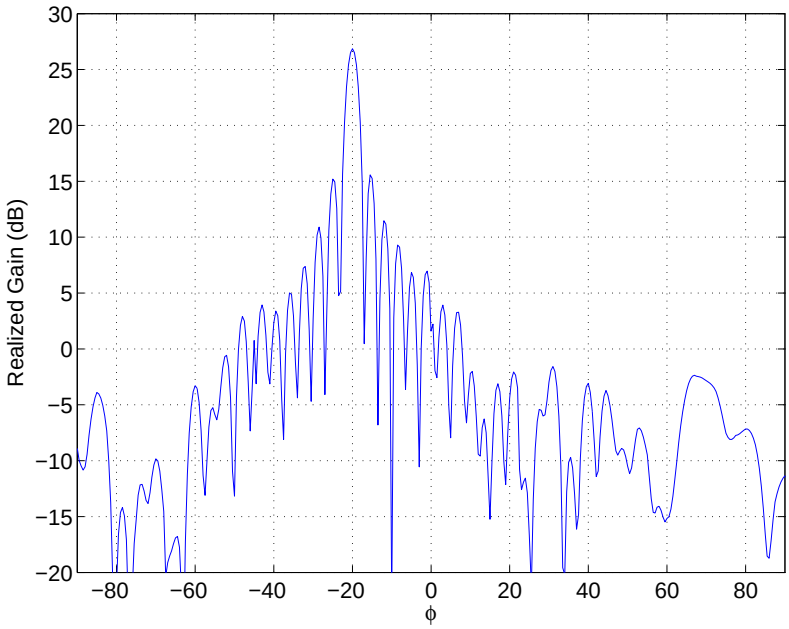

Figure 54 Radiation pattern in horizontal plane using “maximum gain” excitations scanned to -20º.

The input data file contains all data necessary to get the radiation from all elements at one specific frequency. For each element its position, $\mathbf{r}_{el}$, the element normal vector, $\hat{x}_{el}$, and the tangent vector, $\hat{z}_{el}$, by which the polarization is defined is given in global coordinates, see section 3.2. The start, stop and number of angles are given and to get the pattern data at these, evenly spaced directions, the patterns may

have to be interpolated. The radiation pattern data, in the form of real and imaginary parts of the field gain, obtained from the measurements are given in a long table. Since we have not measured all individual elements we make a “guess” of the patterns of some of the elements based on their position in the array. For the faceted array we also use symmetry considerations to choose elements and make a mirror transformation of their patterns.

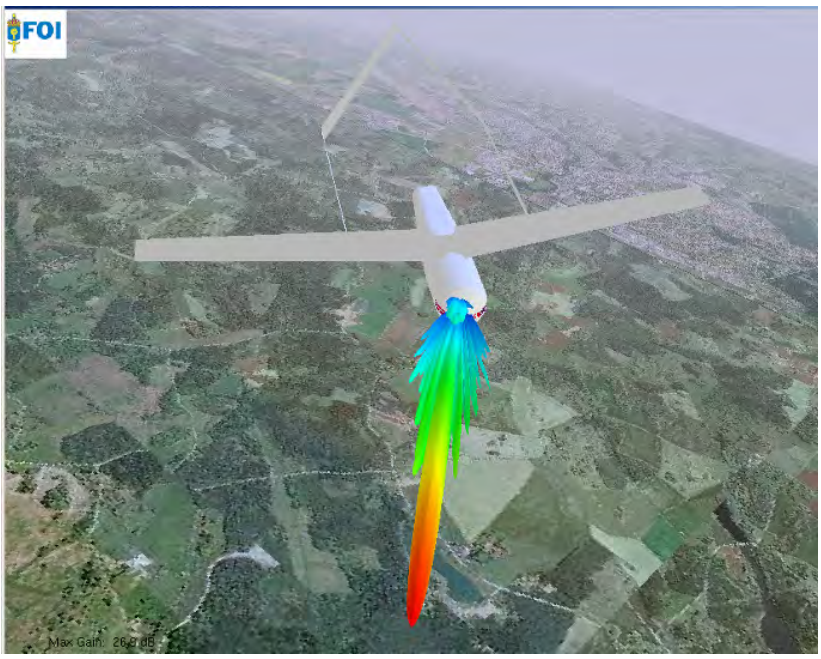

Figure 55 Synthesized antenna beam with maximum gain criteria, using measured element patterns of the experimental faceted antenna array, visualized in the VISCA-tool [4]. The beam is scanned 20º from the nose-on direction, where the gain becomes 27 dBi. The gain is color coded with a 30 dB range.

6 Conclusions

Two different conformal Ku band arrays, one with subarrays in the form of facets and one smoothly curved, having bandwidth about 2 GHz have been built, mounted on an UAV nose mock-up and evaluated experimentally. The smoothly curved array is easier to manufacture but in a full system, with TR modules at each element, the reverse may be true. Patterns of selected elements have been measured and analyzed. Both systematic and a random-like variations can be seen. Since most of the elements in the smoothly curved array are in a more similar environment they have slightly higher pattern quality but the pattern quality of both arrays is considered adequate to produce good array patterns.

7 References

[1] L. Pettersson, T. Martin, L-G. Huss, R. Erickson, O. Lundén, S. Leijon, ”Experimental investigation of a conformal array antenna on a UAV-nose mock-up”, 5th European Workshop on Conformal Antennas, Bristol, UK, 10-11 Sept. 2007.

[2] L. Pettersson, R. Gunnarsson, O. Lundén, S. Leijon, A. Gustafsson, ”Experimental investigation of a smoothly curved antenna array on a UAV-nose mock-up”, ”, EuCAP10, Barcelona, Spain, 12-16 April 2010.

[3] R. Erickson, R. Gunnarsson, T. Martin, L-G. Huss, L. Pettersson, P. Andersson, A. Ouacha, ”Wideband and wide scan smart-skin phased array antennas for small platforms”, EuCAP07, Edinburgh, UK, 11-16 Nov. 2007.

[4] T. Martin, “A visualization tool for conformal antenna arrays on platforma”, 4th European Workshop on Conformal Antennas, Stockholm, Sweden, 23-24 May 2005.

[5] A. C. Ludwig, ”The Definition of Cross Polarization”, IEEE Trans. on Antennas and Propag., pp.116-119, Jan. 1973,

FOI, Swedish Defence Research Agency, is a mainly assignment-funded agency under the Ministry of Defence. The core activities are research, method and technology development, as well as studies conducted in the interests of Swedish defence and the safety and security of society. The organisation employs approximately 1000 personnel of whom about 800 are scientists. This makes FOI Sweden's largest research institute. FOI gives its customers access to leading-edge expertise in a large number of fields such as security policy studies, defence and security related analyses, the assessment of various types of threat, systems for control and management of crises, protection against and management of hazardous substances, IT security and the potential offered by new sensors.

FOI
Defence Research Agency
Information Systems
Box 1165
SE-581 11 Linköping

Phone: +46 13 37 80 00
Fax: +46 13 37 81 00

www.foi.se